Acta Geotechnica
https://doi.org/10.1007/s11440-021-01401-8

RESEARCH PAPER

On the role of joint roughness on the micromechanics of rock fracturing process: a numerical study

Ge Gao[1] · Mohamed A. Meguid[2]

Received: 3 July 2021 / Accepted: 12 October 2021
© The Author(s), under exclusive licence to Springer-Verlag GmbH Germany, part of Springer Nature 2021

Abstract
The deformation process and failure mechanism of rock mass with increased joint roughness subjected to unconfined compression are investigated in this study using discrete element method. A numerical model is developed using soft-bonded particle and validated to realistically replicate the mechanical response of the rock mass. The micro-parameters of the rock material are first determined, and the effects of the joint roughness on the macromechanical response and fracture growth mechanism are then investigated. Analyses are also performed to examine the tensile and shear crack distributions, acoustic emission (AE) characteristics, coordination number, and crack anisotropy to advance the current understanding of the role of joint roughness on the mechanical behavior and deformability of rock mass. The results show that strength and deformability of the jointed rocks are highly dependent on the joint orientation and roughness. Joint roughness is found to restrain the propagation and coalescence of microcracks and AE events from the interlocking of asperities. In addition, the spatial distribution of the contact forces allows for better understanding of the effect of joint inclination angle on the response of the investigated rock samples.

Keywords Acoustic emission · Crack tensor · Joint roughness · Rock fracturing processes · Soft-bonded discrete element model

1 Introduction

The fracture behavior of rock mass is of prime importance to many rock engineering projects, such as deep underground excavations, and stability of natural rock slopes. Rock mass is complex geological medium that may involve features such as fissures, joints, faults, and bedding planes, which strongly affect the performance of engineering structures. The types and origins of discontinuities play a decisive role in the failure of rock mass since existing discontinuities provide planes of weakness on which further deformation can occur [1, 74, 75]. The fracturing process of jointed rock mass is governed by not only the initiation and propagation of individual cracks but also the interaction and coalescence within existing discontinuities. Therefore, knowledge of the fracture behavior of jointed rock mass is necessary to accurately predict rock instability, which leads to improved design.

The fracture behavior and failure mechanism of jointed rock masses under compressive loading have drawn ample attention from both researchers and practicing engineers over the past few decades. Substantial effort has been made to study fracture initiation, propagation, interaction, and eventual coalescence within a rock mass using both experimental and theoretical methods [4, 11, 29, 50, 54, 63–65, 71]. In one of the earliest studies, Brace and Bombolakis [8] found that the eventual failure of a rock sample develops by crack interaction that usually forms a macro-shear fault. Wong and Chau [60] experimentally studied the response of rock samples with flaw

✉ Mohamed A. Meguid
mohamed.meguid@mcgill.ca

Ge Gao
gaoge@sjtu.edu.cn

[1] State Key Laboratory of Ocean Engineering, Shanghai Key Laboratory for Digital Maintenance of Buildings and Infrastructure, School of Naval Architecture, Ocean and Civil Engineering, Shanghai Jiao Tong University, Shanghai 200240, China

[2] Department of Civil Engineering, McGill University, 817 Sherbrooke St. W., Montreal, QC H2A 0C3, Canada

Published online: 28 October 2021

inclination angles ranging from 35° to 75° and identified three main crack coalescence modes: shear mode, mixed shear/tensile mode, and wing tensile mode. Haeri et al. [27] found that the peak strength of rock samples is related to the inclination angle of the cracks.

In general, the orientation, spacing, continuity, and number of pre-existing cracks or joints dominate the deformation and fracture characteristics of rocks [45, 51, 59, 67, 69]. Conducting experiments on rocks with pre-existing cracks and real-time monitoring of opaque rock-like materials are usually challenging [2, 35, 37]. Therefore, numerical analysis seems to be necessary for studying crack propagation and coalescence in rock mass.

Numerical modeling approaches can be classified into two main categories: continuum and discontinuum methods. Continuum methods, including the finite element (FEM) and boundary element (BEM) methods, generally assume continuous, isotropic, and homogeneous medium. Rock damage and failure are assessed using constitutive models such as elasto-plastic or elasto-viscoplastic and damage mechanics models [18]. However, the presence of weak planes, being the source of large deformation and low shear strength, makes the micro-mechanisms developing in a rock mass complex and difficult to characterize using continuum theories [49]. In contrast to continuum methods, the application of the discrete element method (DEM) to simulate jointed rock mass has the following advantages: (i) the failure and fracture development caused by a joint face can be simulated free from the limits of the mesh deformation; (ii) the distribution of actual joint faces can be considered; (iii) the influence of microstructure on the macroscopic behavior can be studied. Therefore, the discrete element method (DEM) constitutes a powerful tool to capture the heterogeneous and anisotropic nature of a rock mass and assess the fracturing behavior and failure mechanism of jointed rock masses [10, 20, 69, 78].

De Silva and Ranjith [15] used discrete element analysis to simulate rock formations with complex joint geometries to study rock mass fracturing mechanisms. It was found that joints create a preferential direction for fracture propagation and cracking generally propagates toward a direction opposite to the joints. Yang et al. [68] modeled uniaxial compression tests of non-persistent jointed rock samples by analyzing the effects of joint gap, dip angle, and persistency. It was concluded that the contact and interaction of joint surfaces have significant effects on the mechanical behavior of jointed rock blocks. Scholtès et al. [52] used discrete element to numerically investigate the effect of discontinuities on the development of fractures in rock-like material. They demonstrated that discontinuities have significant effects on the overall response of the material.

Despite the promising results of the above studies in investigating the behavior of jointed rock of different joint geometries (e.g., orientation, length, spacing, and bridge length) under compressive loadings, most of the reported work was either experimental or numerical performed on rock mass of single or multiple sets of smooth non-persistent joints. Indeed, natural rocks are characterized by undulated and rough joint surfaces that play an important role in the damage evolution and fracture mechanism of the rock mass [25, 44]. Therefore, this study aims to shed more light on the effect of joint roughness on the mechanical behavior of jointed rock mass subjected to uniaxial compression. First, a validation is performed by comparing the results of the developed numerical models with laboratory data obtained for discontinuous rough-jointed rock samples. The non-persistent rough joints with various degree of joint roughness are produced on the basis of the selected standard joint roughness profiles proposed by Barton and Choubey [7] who introduced the joint roughness coefficient (JRC) to quantify rock joint roughness according to the shear strength model ($\tau = \sigma_n \tan\left[\mathrm{JRC}\,\log_{10}\left(\frac{\mathrm{JCS}}{\sigma_n}\right) + \phi_b\right]$, where τ is the peak shear strength, σ_n is the effective normal stress, JCS is the joint wall compressive strength, and ϕ_b is the basic friction angle). The well-known joint roughness standard profiles are then proposed for JRC values that range from 0 to 20. Second, the mechanical response at the macroscopic level, including peak stress, deformation modulus, and cracking process, is compared with the measured values. Third, detailed micro-mechanical analysis is carried out to gain new insights into fracture growth, and evolution of energy transition and coordination number within the tested rock samples. In addition, the original application of acoustic emission characteristics and crack tensor analyses helps explaining the fracturing process and failure mechanism of rock masses.

2 Model description

Discrete element (DEM) is generally viewed as a method that allows for finite displacements and rotations of discrete bodies and updates contacts automatically [12]. The original application of DEM by Cundall and Strack [13] is aimed to study the behavior of granular material and blocky rock systems. Nowadays, DEM is broadly used in geomechanics from soil to rock masses with applications in different areas, including, rock engineering, soil mechanics, geohazards, and geotechnical engineering [21, 24, 32, 36, 61, 66, 73].

The most widely used contact model related to rock mechanics in the DE analyses is the Bonded-Particle Model (BPM) proposed by Potyondy and Cundall [49].

Nonetheless, Ma and Huang [42] pointed out that using the standard BPM with elastic-perfectly brittle contacts leads to macro-scale strength ratio (σ_c/σ_t) that is much lower than that of real rocks, i.e., the uniaxial compressive strength (σ_c) and tensile strength (σ_t) cannot be matched simultaneously. However, a realistic strength ratio is critical to accurately interpret failure mechanism of a rock mass at the macro-scale level [43, 53].

Compared to previous studies that used BPM to simulate rock mass or rock-like materials, a novel aspect of this study is that a new contact model (soft-bond model) implemented in PFC 6.0 [33] that accounts for the softening regime in the contact bond strength is applied. The model is capable of reproducing the expected high UCS to tensile strength ratio, internal friction angle, and the nonlinear strength envelope. In an unbonded state, the soft-bond contact model behaves essentially similar to that proposed by Jiang [34] with the ability to transmit both force and moment at the contact point, with frictional strength parameters that limit the shear force, bending and twisting moment.

2.1 Modeling jointed rock mass

The soft-bond model allows for the rock material to be simulated using a statistically generated assembly of bonded particles at the micro-scale level. The introduction of smooth-joint contact model in the soft-bond particle systems provides the DEM model with the ability to simulate the mechanical behavior and fracture mechanism of jointed rock mass under uniaxial compressive loading. Discrete element modeling of jointed rock masses comprises four typical components [56]:

1. Discrete spherical/disk elements of finite radius r, mass density ρ, and friction coefficient μ. These discrete particles obey Newton's laws of motion and can interact when they are either in contact or bonded.
2. The force–displacement law of the soft-bond model updates the contact forces and moments:

$$\mathbf{F_c} = \mathbf{F} + \mathbf{F^d} \tag{1}$$

$$\mathbf{M_c} = \mathbf{M} \tag{2}$$

where $\mathbf{F}$ is the linear force, $\mathbf{F^d}$ is the dashpot force, and $\mathbf{M}$ is the linear moment. The linear force is resolved into normal and shear force, and the linear moment is resolved into a twisting and bending moment:

$$\mathbf{F} = -F_n\hat{\mathbf{n}}_\mathbf{c} + \mathbf{F}_s \tag{3}$$

$$\mathbf{M} = M_t\hat{\mathbf{n}}_\mathbf{c} + \mathbf{M_b}\ (\text{2D model: } M_t \equiv 0) \tag{4}$$

where $\hat{\mathbf{n}}_\mathbf{c}$ is the unit vector that defines the contact plane.

3. Soft Bonds may carry force and moment ($\mathbf{F}$ and $\mathbf{M}$) and provides two distinct responses depending on its bonding state (see Fig. 1). When unbonded, it provides linear elastic behavior and frictional with rolling resistance. When bonded, the soft-bond model becomes similar to the linear parallel bond model with tensile softening, which is characterized by linear elastic behavior until either the shear or tensile strength limit is reached. If the shear strength limit is exceeded, the bond breaks making the model unbonded. However, if the tensile strength limit is exceeded, contrary to the linear parallel bond model, the bond is not removed and instead the model enters a softening regime (see Fig. 1b) until the bond stress reaches a threshold value where the bond breaks making the model unbonded.

The increments of elastic force and moment are given by

$$F_n := F_n + k_n A\Delta\delta_n \tag{5}$$

$$\mathbf{F_s} := \mathbf{F_s} - k_s A\Delta\boldsymbol{\delta}_s \tag{6}$$

where $\Delta\delta_n$ and $\Delta\boldsymbol{\delta}_s$ are, respectively, the relative normal-displacement and shear-displacement increments.

$$\overline{M}_t := \begin{cases} M_t - k_s J\Delta\theta_t, & \text{3D} \\ 0, & \text{2D} \end{cases} \tag{7}$$

$$\mathbf{M_b} := \mathbf{M_b} - k_n I\Delta\boldsymbol{\theta}_\mathbf{b} \tag{8}$$

$\Delta\theta_t$ and $\Delta\boldsymbol{\theta}_\mathbf{b}$ are the relative twist-rotation and bend-rotation increments, respectively; A, I, and J are the area, moment of inertia, and polar moment of inertia of the cross section, respectively. In two dimensions, $A = 2Rt$, $I = \frac{2}{3}R^3t$, and $J = 0$.

Updating the maximum normal (σ, $\sigma > 0$ is tension) and shear (τ) stresses at the bond periphery using:

$$\sigma = \frac{F_n}{A} + \beta\frac{\|\mathbf{M_b}\|R}{I} \tag{9}$$

$$\tau = \frac{\|\mathbf{F_s}\|}{A} + \begin{cases} \beta\dfrac{|M_t|R}{J}, & \text{3D} \\ 0, & \text{2D} \end{cases} \tag{10}$$

with $\beta \in [0, 1]$.

If the bond is intact and the maximum normal stress at the bond periphery exceeds the bond tensile strength ($\sigma > \sigma_c$), then the bond enters the softening regime, and the maximal bond elongation is set to:

$$l^* = l_c(1.0 + \zeta) \tag{11}$$

$$\text{with} \quad l_c = \frac{F_n}{k_n A} + \beta\frac{\|\mathbf{M_b}\|R}{k_n I} \tag{12}$$

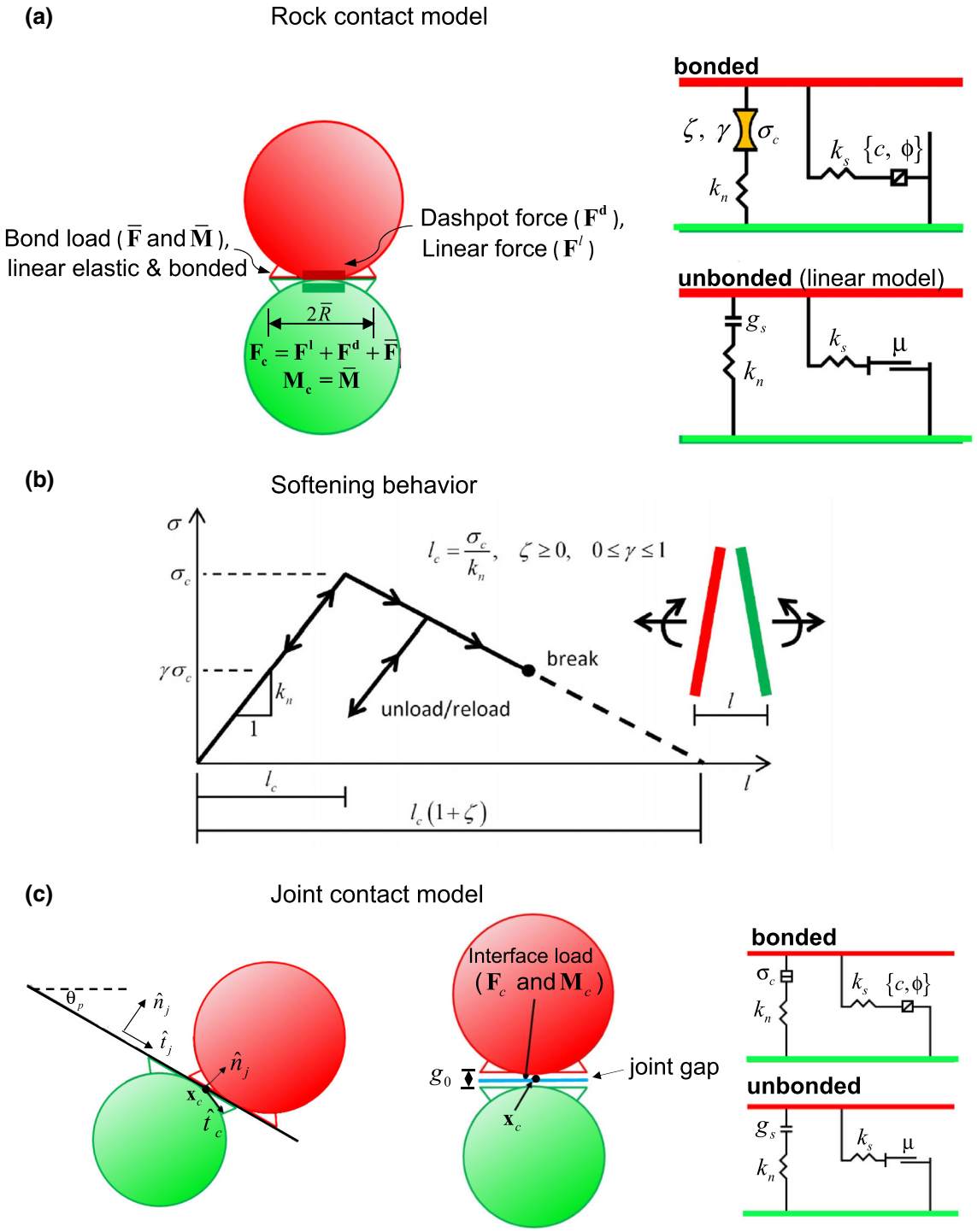

Fig. 1 Behavior and rheological components of: **a** soft bond model; **b** softening behavior of the soft bond model; **c** smooth-joint model

where l_c is the critical bond elongation (at peak strength) and ζ is the bond softening factor.

If the bond is within the softening regime, the normal stress at the bond periphery is checked against the softening envelope as follows:

The maximum stress is given by:

$$\sigma^* = \frac{\sigma_c(l^* - l)}{\zeta l_c} \tag{13}$$

where the current bond elongation l is expressed as:

$$l = l_c + \delta l + R|\delta\boldsymbol{\theta}_{\mathbf{b}}| \tag{14}$$

where δl is a measure of the bond elongation since softening started:

$$\delta l := \delta l + \Delta\delta_n \tag{15}$$

and $|\boldsymbol{\delta\theta}_\mathbf{b}|$ is a measure of the accumulated bending since softening started.

Tensile failure is first checked to determine if the bond is within the softening regime and $\sigma \leq \sigma_c\gamma$, then the bond breaks in tension, and $\mathbf{F} = 0$, $\mathbf{M} = 0$. If the bond has not failed in tension, then shear failure is assessed. The shear strength $\overline{\tau}_c = -\sigma \tan \overline{\phi} + \overline{c}$, where $\sigma = \frac{\overline{F}_n}{A}$ is the average normal stress acting on the bond cross section. If the shear strength limit is exceeded ($\overline{\tau} > \overline{\tau}_c$), then the bond breaks in shear.

4. *Joints*: With the introduction of the smooth joint contact model, the bonded-particle discrete element model with embedded smooth joints allows for the generation of an equivalent anisotropic jointed rock mass. After generation of the joint plane, a smooth joint is assigned to the particle contacts with centers located on the opposite sides of the joint plane. At these contacts, the bonds are removed and smooth joints are defined in a direction parallel to the joint plane (see Fig. 1c). Particles intersected by a smooth joint may overlap and pass through each other rather than be forced to move around one another.

A smooth joint can be envisioned as a set of elastic springs uniformly distributed over a circular cross section, centered at the contact point and oriented parallel to the joint plane. The area of the smooth-joint cross section is given by:

$$A = \pi R^2 \tag{16}$$

with $R = \lambda \min(R^{(1)}, R^{(2)})$.

where $R^{(1)}$ and $R^{(2)}$ are the radii of the two contacting entities (disk/sphere).

The force–displacement law for the smooth-joint model updates the contact forces (Fig. 1b) as given by:

$$\mathbf{F_c} = \mathbf{F},\ \mathbf{M_c} \equiv 0 \tag{17}$$

where $\mathbf{F}$ is the smooth-joint force. The force is resolved into normal and shear forces:

$$\mathbf{F} = -F_n\hat{\mathbf{n}}_\mathbf{j} + \mathbf{F_s} \tag{18}$$

Updating the normal and shear forces:

$$F_n = (F_n)_0 + k_n A \Delta\overset{\frown}{\delta}{}_n^e \tag{19}$$

$$\mathbf{F}_\mathbf{s}^* = (\mathbf{F_s})_0 - k_s A \Delta\overset{\frown}{\delta}{}_s^e \tag{20}$$

where $(F_n)_0$ and $(\mathbf{F_s})_0$ are the smooth joint normal and shear forces, respectively, at the beginning of the time step; $\Delta\overset{\frown}{\delta}{}_n^e$ and $\Delta\overset{\frown}{\delta}{}_s^e$ are the elastic portions of the normal and shear displacement increments.

The shear strength is also computed as:

$$F_s^\mu = -\mu F_n \tag{21}$$

In the unbonded smooth joint model, the shear force is updated using:

$$F_s = \begin{cases} \mathbf{F}_\mathbf{s}^*, \left\|\mathbf{F}_\mathbf{s}^*\right\| < F_s^\mu \\ F_s^\mu(\mathbf{F}_\mathbf{s}^*/\left\|\mathbf{F}_\mathbf{s}^*\right\|) \end{cases} \tag{22}$$

When $\|\mathbf{F_s}\| = F_s^\mu$, the slip state is active, and the contact is sliding. In this case, shear displacements result in an increase in normal force due to dilation:

$$F_n = F_n + \left(\frac{\mathbf{F}_\mathbf{s}^* - F_s^\mu}{k_s}\right) k_n \tan\psi \tag{23}$$

2.2 Model calibration

To build a reliable discrete element model that realistically reflects the mechanical behavior of a rock mass, the micro-mechanical properties to be assigned to the particles and soft bonds are needed. However, these properties cannot be measured directly using laboratory experiments; thus, extensive model calibration is unavoidable. This requires an iterative process using different micromechanical properties, until the numerical model captures the measured response. The calibration is conducted based on the uniaxial compression and Brazilian tests with the aim of finding appropriate micro-parameters that match the three key macroscopic properties, i.e., uniaxial compressive strength (UCS), Brazilian tensile strength, and elastic modulus. Schematic diagrams that show the experimental setups used by Asadizadeh et al. [3] are summarized in Table 1.

2.2.1 Model calibration for intact rock

The experimental results reported by Asadizadeh et al. [3] on intact rocks are first simulated to calibrate the material parameters needed for the soft-bond model. This starts with the generation of a dense packing of nonuniform and well-connected grain assembly with a specified nonzero material pressure, and the installation of soft bonds at grain–grain contacts.

2.2.1.1 Uniaxial compression (UCS) tests A polyaxial vessel consisting of frictionless walls, 300 mm in width and 300 mm in height, is constructed to match the dimensions of the rock sample. Subsequently, an assembly of grains with diameters satisfying a uniform size distribution ($R_{\max}/R_{\min} = 1.66$) is generated, and allowed to

Table 1 Schematic diagrams of testing devices

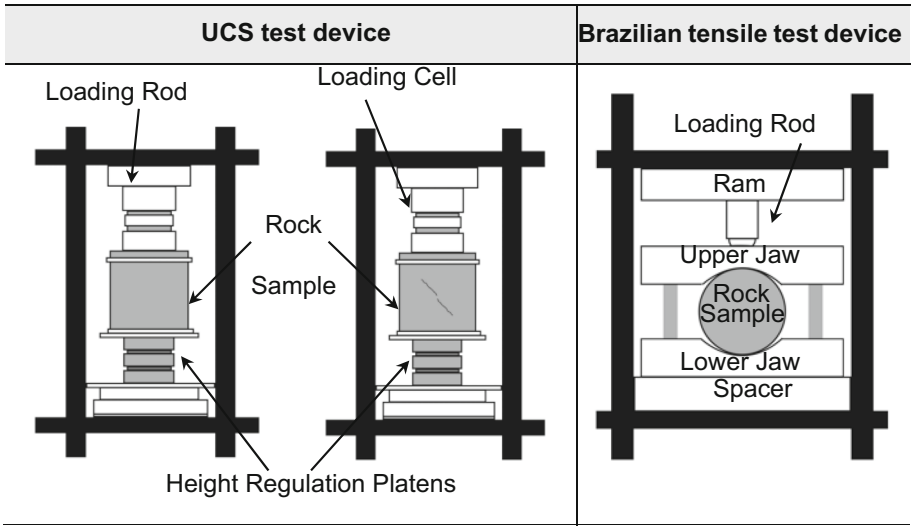

Note: These schematic diagrams are made based on the experimental work of Asadizadeh et al.[3]

rearrange into a packed state under conditions of zero friction until static-equilibrium is reached. The material friction coefficient is set to the particles, and the soft bonds are then introduced, and the final material properties are assigned to the grain–grain contacts. In this case of loading, the axial walls act as loading platens, and the radial walls are moved away from the specimen and kept motionless. Axial pressure is applied by activating the servomechanism with a pressure boundary condition in the axial direction and a velocity boundary condition of zero in the radial direction. Particle contact modulus (E_c), particle normal to shear stiffness ratio (k_n/k_s) are varied to match the measured Young's modulus of the intact rock materials.

2.2.1.2 Brazilian tensile strength (BTS) tests These tests are performed on a cylindrical sample, 300 mm in diameter, oriented such that the loading axis coincides with the cylinder radial direction specimens. Likewise, axial walls that act as loading platens are created. The particulate system with the same particle size distribution similar to that used in simulating the uniaxial compression tests is generated for the Brazilian tests and brought to static equilibrium. The loading phase is activated by moving the axial walls at the specified strain rate, and the peak axial force is used to determine the tensile strength using:

$$\sigma_B = \frac{|F_a|_{\max}}{\pi R t} \tag{24}$$

where $|F_a|_{\max}$ is the peak axial force, and R and t are the radius and thickness of the disk, respectively.

UCS and BTS results are then matched by varying the normal and shear strength of the soft bond, as well as the softening factor. The computed stress–strain response is compared with that measured in the laboratory for intact rocks under unconfined compression as depicted in Fig. 2a. The BTS results shown in Fig. 2b are used to calibrate the macro-scale strength ratio, which is estimated at 22.97/3.43 = 6.7. The calibrated values of the microscopic parameters are listed in Table 2. It should be pointed out that softening is activated in this case by setting a value of 30 for the softening factor, and a value of 0.0 for the tensile strength softening factor. This means that once the tensile strength is reached at a specific contact, the contact enters a softening regime with a softening stiffness that is 1/30th of the loading stiffness and breaks only if the tensile force reaches 0.0. In addition, as suggested by Itasca [33], the bending and twisting friction multipliers are set to 1.0. Based on the comparison of the calculated and measured results in Fig. 2, it can be concluded that the microproperties obtained using the described calibration process ensure that the model reasonably predicts the response of the intact rock samples.

2.2.2 Model calibration for rock mass

After the response of the intact rock is validated, rock mass models need to be created to reproduce the measured response with non-persistent rough joints subjected to uniaxial compression. The rock sample with non-persistent rough joints JRC profile of 14-16 used in the laboratory

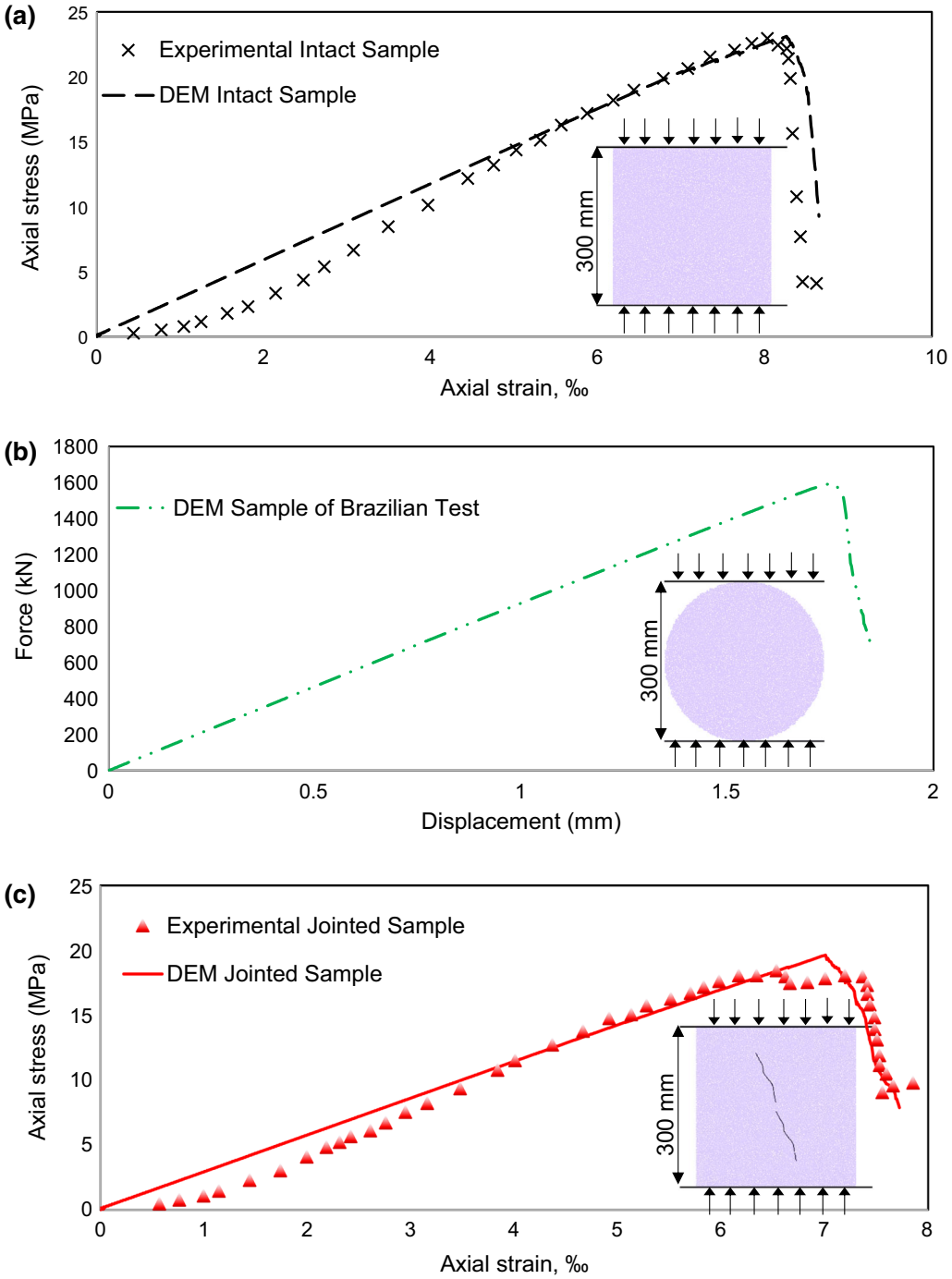

Fig. 2 Calculated and measured responses: **a** intact rock sample under uniaxial compression; **b** intact rock sample under diametral compressive loadings; **c** jointed rock sample under uniaxial compression

experiments [3] is replicated using discrete element analysis (see Table 3). In this case, there is a need to identify the corresponding microproperties for the smooth joint (SJ) contact model that has six essential parameters: joint normal stiffness (k_n^{sj}), shear stiffness (k_s^{sj}), joint tensile strength (σ_t^{sj}), joint cohesion (c^{sj}), joint friction (μ^{sj}), and dilation angle (ψ). Considering that the joint surfaces used in the laboratory experiments are cohesionless and clean-cut, σ_t^{sj},c^{sj} and ψ values are all set to 0 in the model. Joint normal stiffness (k_n^{sj}) is determined by adjusting its value until normal stiffness value consistent with the laboratory results is achieved. As suggested by Huang et al. [30], the k_n^{sj}/k_s^{sj} ratio is taken as 2 in this study. It is worth mentioning that, compared to the calculated linear elastic

Table 2 Numerical parameters used in the discrete element analysis

Item	Micromechanical properties
Rock	
Ball-ball contact effective modulus	3.35 GPa
Ball stiffness ratio (k_n/k_s)	1.5
Ball friction coefficient	0.7
Bending Friction multiplier	1.0
Twisting Friction multiplier	1.0
Soft bond tensile strength	4.01 MPa
Soft bond cohesion	17.16 MPa
Softening factor	30
Softening tensile strength factor	0
Joint set	
Smooth joint normal stiffness (k_n^{sj})	400 GPa
Smooth joint shear stiffness (k_s^{sj})	200 GPa
Smooth joint friction coefficient	0.7
Smooth joint tensile strength (σ_t^{sj})	0 MPa
Smooth joint cohesion (c^{sj})	0 MPa
Smooth joint dilation angle (ψ)	0°

deformations, nonlinear concaving response was measured up to around 4‰ strain for both the intact and jointed samples (Fig. 2a,c). This reflects that under uniaxial compression, most of the tested rock samples experienced an initial crack closure phase, which is attributed to the closure of the natural flaws or the stress-induced cracks resulting from the coring process. This initial phase is hard to replicate numerically due to the unbreakable and undeformable nature of the particles. The generated rock material is generally homogeneous, isotropic with well-connected granular system with no pre-existing defects [38, 48, 53]. Additionally, the emergent stress-variations around the peak stress state (see Fig. 2c) are associated with more pronounced crack coalescences happening in the experiments [3]. This can also be attributed to the intrinsic limitation in the basic formulation of discrete element method as the circular-based particles are rigid and unable to crack or crush under the applied loads [17, 49, 52, 70]. Despite these shortcomings, the macro-response captured by the model for the jointed samples shows an overall agreement with the experimental results, as presented in Fig. 2c.

2.2.3 Rock mass configuration

Once the discrete element models are validated, the mechanical behavior of the rock masses embedded with various configurations of non-persistent rough joints that have 100 mm in length, 17.5 mm bridge length, and inclination angle of 67.5° is investigated (see Table 3). In addition to JRC 14-16 jointed samples, three more rock samples with rough joints that correspond to JRC profiles of JRC 2-4, JRC 10-12, and JRC 18-20 are created. By doing so, additional data can be generated to supplement laboratory tests and capture the details of the rock fracturing process and failure mechanism. Therefore, this numerical study has the merits of investigating both the macroscopic response and microscopic information associated with damage evolution of rough-jointed rock masses. A detailed description of the jointed rock configuration is given in Table 3.

3 Results and discussion

With the verified mechanical parameters, a series of discrete element analysis is performed to model unconfined compression tests on jointed rock samples with increasing degree of joint roughness. This allows for the deformability and failure mechanism of the rock to be investigated at both the micro- and macro-scale levels, including stress–strain responses, failure modes, acoustic emission information, energy budgets, coordination number, crack tensor, and crack anisotropy distributions. In addition, microstructure interpretation is also made to evaluate the effect of joint inclination angles on the response of the rock system.

3.1 Damage and fracturing processes

3.1.1 Mechanical response and acoustic activity

The stress–strain relationships as well as the number of microcracks and acoustic events generated for rocks of different degree of joint roughness under uniaxial compression are presented in Fig. 3. The following observations are obtained:

(1) Joint roughness has significant effects on the deformation behavior, such as stiffness and peak strength. More precisely, significant increase in stiffness and peak strength is found with the increase in joint roughness, i.e., for rock samples with JRC profiles of 2-4, 10-12, 14-16, and 18-20, the peak strengths reach 15.1, 17.5, 19.6 and 21.5 MPa with axial strain arriving at 6.84, 6.81, 7.01, and 7.79 ‰, respectively. In addition, the elastic moduli of these jointed rock samples with the selected JRC profiles are found to be about 2.83, 2.85, 2.87 and 2.88 GPa, respectively.

(2) The three stages representing the stress–strain response of the modeled rock sample are identified:

Stage I (initiation): This stage corresponds to the

Table 3 Configurations of modeled rock blocks

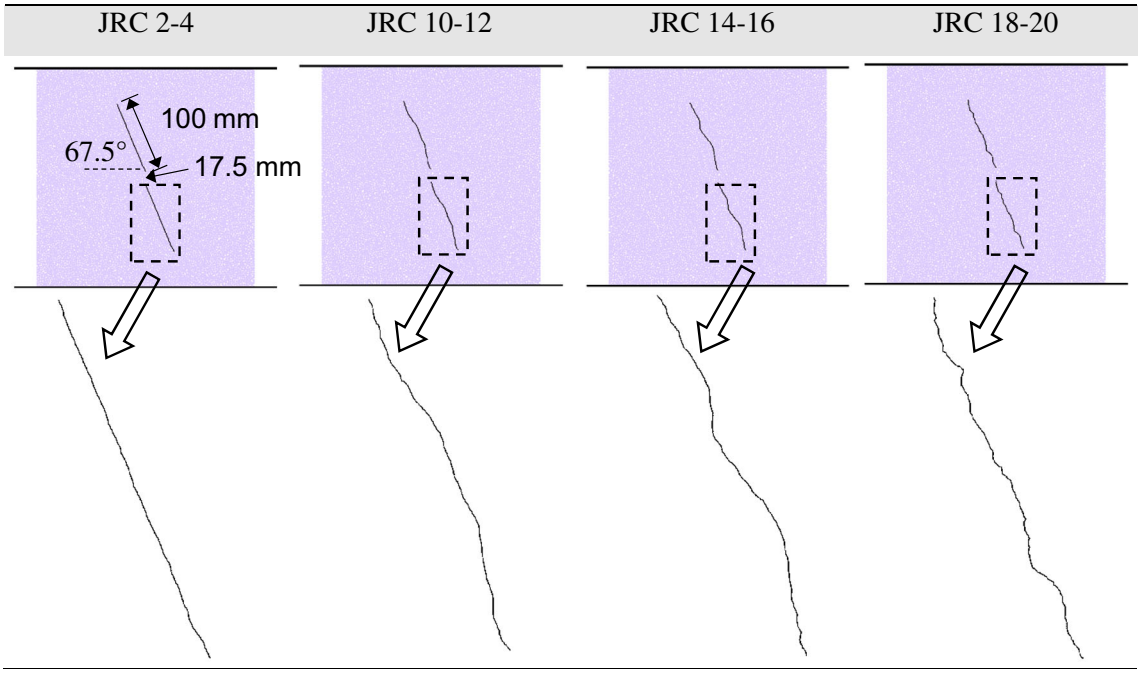

quasi-elastic deformation and is characterized by increasing rock strength following linear stress–strain relationship. This initial stage of the UCS experiment is clearly delineated by low microcracking activity.

Stage II (nucleation): this stage corresponds to an axial strain range where the growth of microcracks is in a slow and steady progress. This begins with the introduction of nonlinearity in the stress–strain behavior of the sample until peak stress is attained. With the increase in applied strains, more damage is accumulated and acoustic energy emits resulting in an increase in the acoustic event count. In addition, this stage is characterized by increasing rock strength and decreasing slope of the stress–strain curve, corresponding to growth of local microcracking events within the rock sample. Compared with rock samples embedded with rough and irregular joints, greater number of microcracks are generated in rock samples with smooth and planar joints during this stage, which are reflected by more pronounced deviation of the stress–strain curve with respect to its initial slope. This is attributed to the fact that the planar and smooth joints are much more favorable for the occurrence of accelerating amount of bond breakages, which causes permanent damage and contributes to the nonlinearity. These results are in line with the conclusions made by Walton et al [58].

Stage III (rupture): This stage corresponds to an axial strain range associated with vertical growth in the number of microcracks and sharp increase in the AE count, which defines the post-peak stress–strain behavior of the rock sample. Stage III is characterized by decreasing rock strength with strain softening behavior and increase in volumetric strain with rapid dilatancy.

Based on the response observed in this stage, with increasing degree of joint roughness, the rock sample is essentially exhibiting brittle behavior with repaid decrease in strength without significant change in the resulting strains. Furthermore, with the increase in joint roughness, the stress drops quickly and the episode of microcracking becomes more intense. In contrast, the stress–strain relationship for the case of smooth and planar joints does not exhibit rapid drop following peak strength, implying that these samples show enhanced ductile response.

(3) When the joint is rough and highly undulated, the AE activities of the jointed rock samples mainly follow stage III and seldom appear at stages I and II (Fig. 3c, d). When the joint roughness declines to a lower degree, the concentration of AE activity appeared early and are relatively pronounced in Stage II (see Fig. 3a, b). It is worth noting that the

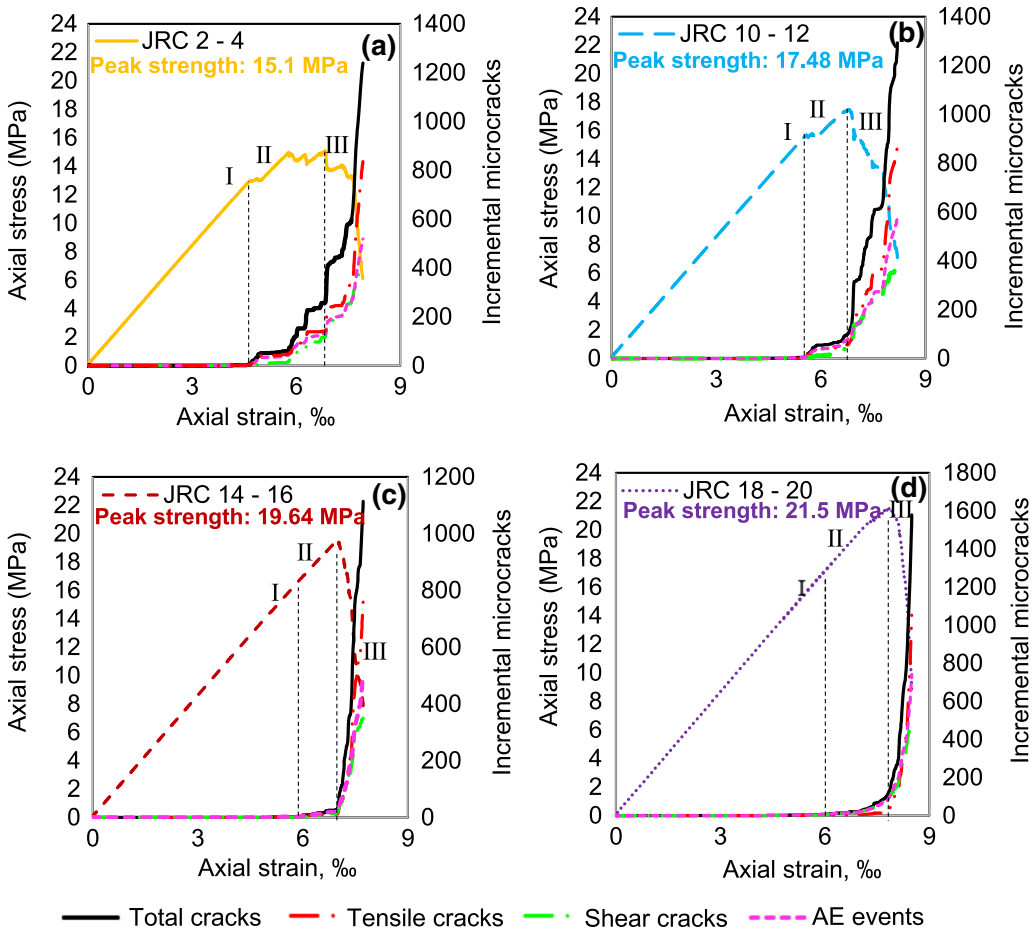

Fig. 3 Stress–strain responses of: **a** JRC 2-4, **b** JRC 10-12, **c** JRC 14-16, and **d** JRC 18-20 rock samples

cumulative AE counts for the rock samples with smooth and planar joints are generally smaller than those with rough and irregular joints, e.g., 517 AE counts are found for JRC 2-4 rock samples in contrast to 741 AE counts for JRC 18-20 samples.

(4) With the continuous increase in the degree of joint roughness, i.e., from smooth (JRC 2-4) and rough planar joints (JRC 10-12) to rough undulating (JRC 14-16), and irregular joints (JRC 18-20), the evolution of the microcracks transits from a step-wise manner characterized by an accumulation of cracks at a relatively slower rate to a surge with rapid increment of cracks. This is mainly due to the fact that the localization and coalescence of freshly formed cracks are countered by the rock mass to disaggregate along the smooth and planar joints.

3.1.2 Fracture growth mechanisms

Stage 1 (initiation): is characterized by low microcracking activity. Initial deformation of these jointed rock samples is defined in terms of distributed tensile and shear microcracking, marking the onset of inelastic deformation. The microcracking is found to mainly concentrate in the rock bridge areas of JRC 2-4 and JRC 10-12 samples that have smooth planar and rough joints, respectively. Conversely, microcracking particularly occurs along rough and irregular asperities, as presented in Fig. 4.

During the nucleation stage, deformation in JRC 2-4, 10-12, and 14-16 rock samples is progressively localized with growth of shear and tensile microcracks, arising from the tips of the non-persistent joints. At the end of the nucleation stage, i.e., at the peak stress state, the pre-existing rough joints are progressively linked through the emergence of microcracks, and the rock bridges are cut by the gradual accumulating of fractures. Fracture nucleation in these three rock samples involves both shear and tensile microcracking. Nevertheless, shear microcracking is the dominant nucleation mechanism in the JRC 18-20 rock sample, and the associated damage characterized by microcracking predominantly localized along rough and irregular asperities and homogenously distributed inside the intact rock matrix.

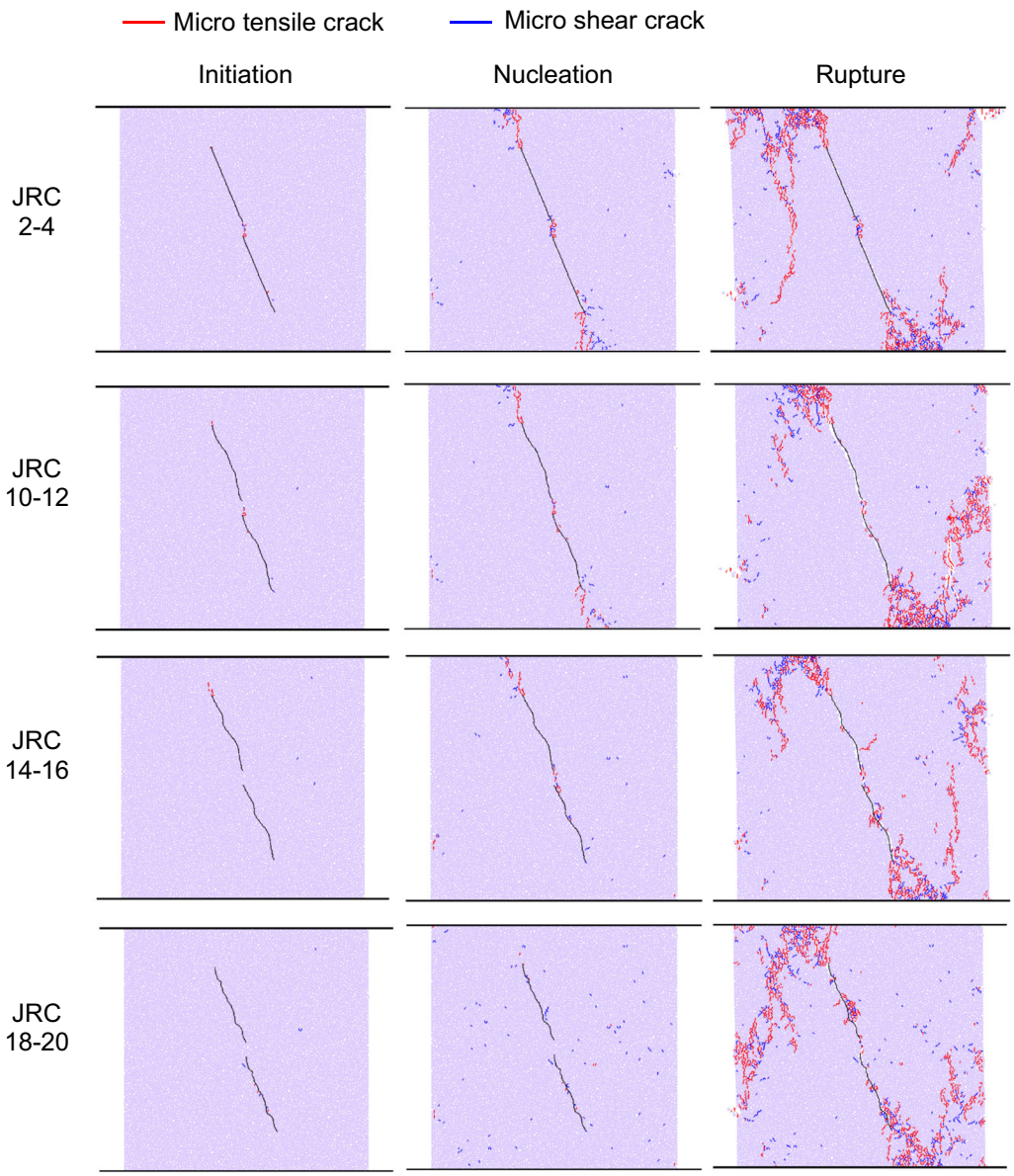

Fig. 4 Distribution of microcracks within the jointed rock samples for the distinct three stages

After the peak stress state, as deformation begins to concentrate, pre-existing and newly generated microcracks merge and propagate into a through-going shear rupture. In accordance with damage mechanics, the episode of intense microcracking leads to significant stress drop, particularly for the cases of JRC 14-16 and JRC 18-20 rock samples. As shown in the rose diagrams in Fig. 5, tensile microcracks have a preferential vertical orientation, which is parallel to the direction of the major principal stress. This agrees with the observation made by Hazzard et al. [29] for axially loaded rock samples. In addition, the distribution of the shear crack orientation developing during the process of macroscopic shear rupture can be associated with the antithetic (oblique to the major shear band) and synthetic (parallel to the major shear band) cracks, which is also consistent with the observations made by Desbois et al. [14], and Dinç and Scholtès [17].

Visual representation of tensile and shear stresses acting on the periphery of the soft bonds is constructed in Fig. 6 to provide micromechanical explanation to the origins of damage and distributions of the developed microcracking in rocks with increasing degree of joint roughness. Figure 6 shows that strong tensile stress acting on the periphery of soft bonds predominantly oriented parallel to the loading direction, which corresponds to the orientation of tensile cracks. Likewise, the shear stresses acting on the periphery of the soft bonds show preferential orientations that are directly related to the orientation of the shear microcracks

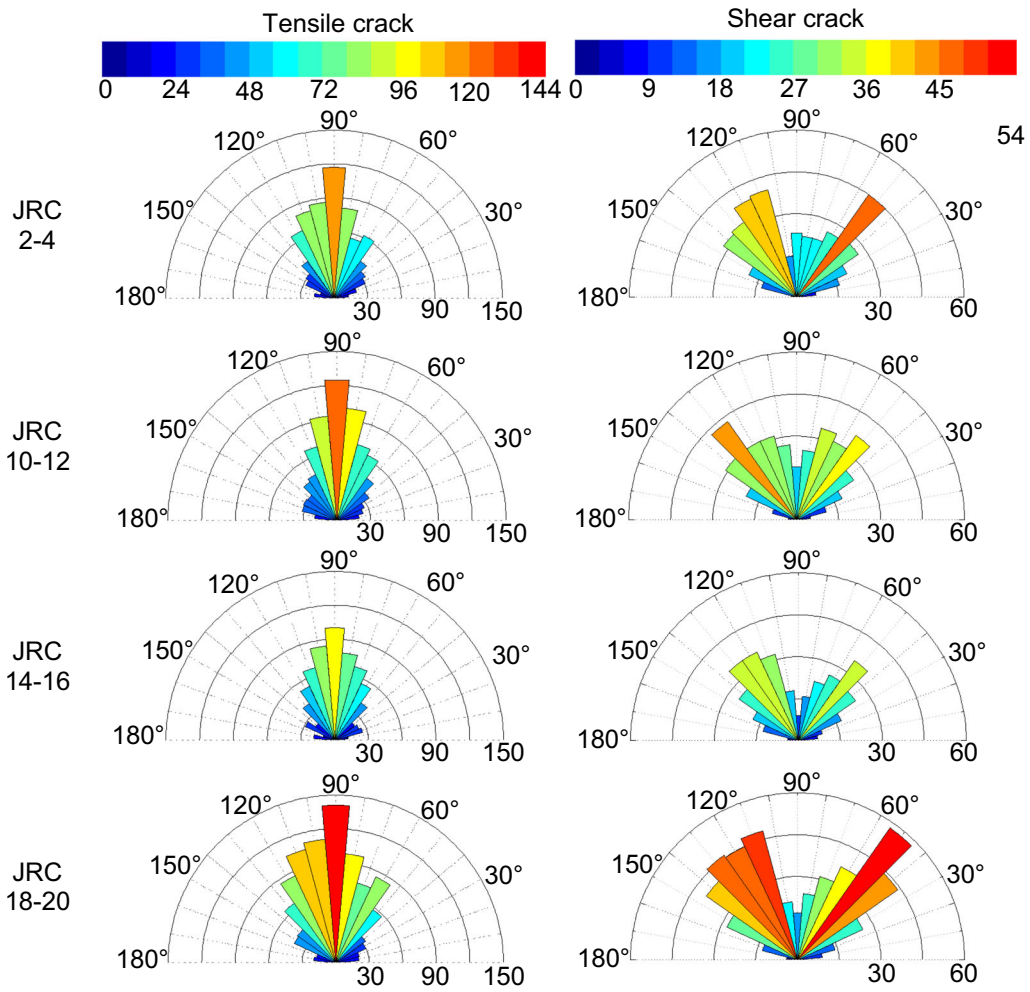

Fig. 5 Orientation distribution of tensile/shear microcracks in the jointed rock samples at the final damage stage. Note: The hue scale indicates the number of tensile/shear microcracks

being either orientated subparallel or sub-perpendicular to the shear band. It is found that the higher the degree of roughness of the joint surface, the larger the magnitude of stresses acting on the periphery of the soft bonds. This can be explained by the fact that undulating and irregular rough joint planes are prone to stress concentration related to the coalescence of emergent microcracks.

It is worth noting that the localized tensile and shear microcracks along the pre-exiting rough joints are only observed for JRC 14-16 and JRC 18-20 rock samples, which have much larger undulating and irregular morphologies compared to the remaining samples. This is explained by the fact that geometric irregularities (waves) of joints with higher degree of roughness are favorable for the nucleation of microcracks due to the asperities of large amplitudes and inclination angles. This accords well with the observations of Camones et al. [9] where irregular surfaces resulted in higher chances of forming microcracks within the rock blocks.

3.1.3 Energy budget during rock fracturing process

The energy evolution mechanism is closely related to the progressive localization of damage inside the rock. Therefore, understanding the energy input, elastic strain energy accumulation, energy dissipation and release is helpful in gaining deeper micromechanical insight into the rock fracturing and failure mechanisms. These energy terms are specified by the work input at the boundary dE_W, body work dE_b done by gravity, strain energy dE_s stored in the linear springs, kinetic energy dE_k, frictional dissipation energy dE_f, damping dissipation energy dE_d, and fracture energy E_{frac}. The cumulative energy released by all bond breakage in the modes of tensile and shear fractures can then be calculated. In this study, the body work dE_b is equal to zero as the gravity acceleration was set to zero.

For a balanced energy budget, the sum of recoverable strain energy and irrecoverable plastic dissipation energy

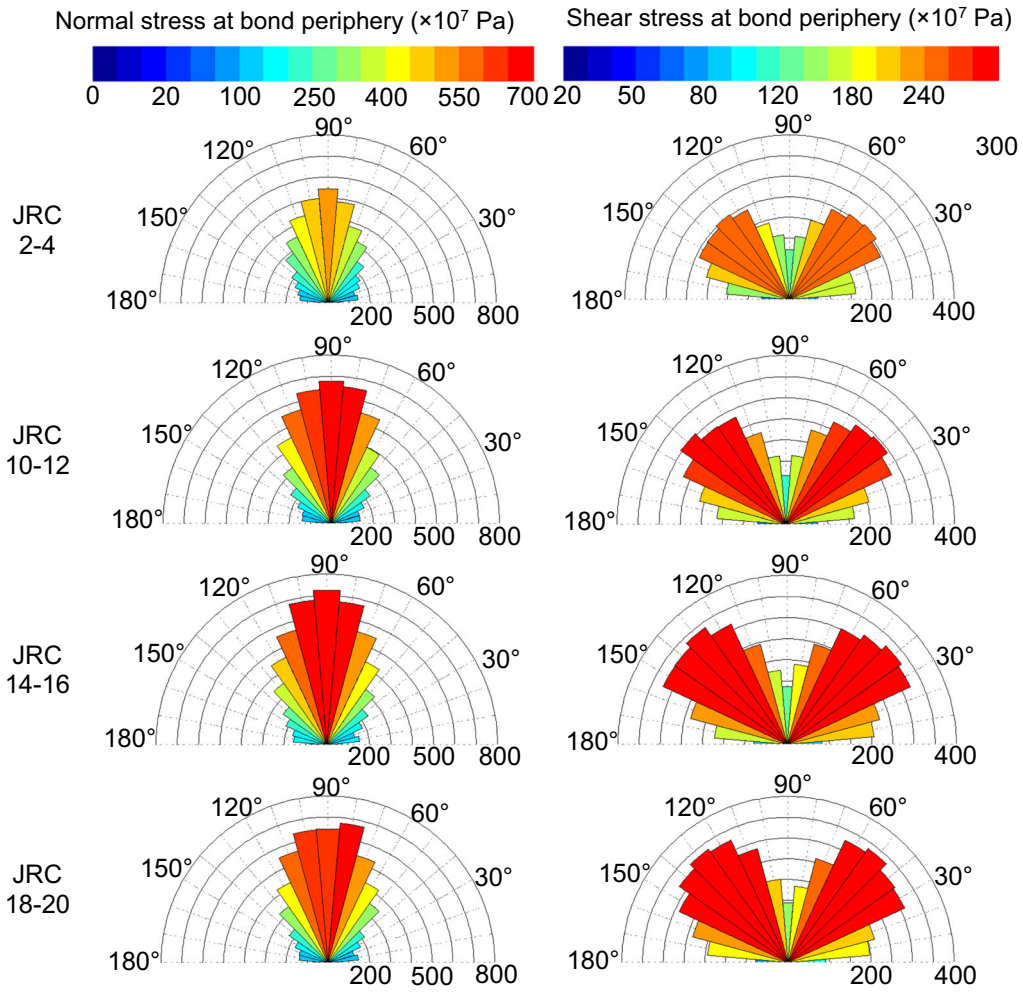

Fig. 6 Orientation distribution of normal/shear stress acting at the periphery of the soft bonds within the jointed rock samples at the final damage stage

will equal the external mechanical work applied to the system:

$$dE_W = dE_s + dE_k + dE_f + dE_d + dE_{\text{frac}} \tag{25}$$

It is noteworthy that the profile of the incremental strain energy has an overall good agreement with the stress–strain curve for each investigated jointed rock samples. At the pre-peak stage, i.e., during the stages of initiation and nucleation, both the external mechanical work applied to the system (dE_W) and strain energy (dE_s) relationships show upward-concave and nonlinear evolution features. The energy absorbed by the rock is mainly stored in the form of strain energy. As shown in Fig. 7, during the initiation stage, the trends of total and elastic strain energy are basically overlapping. After reaching the coalescence stage, the rock enters a nonlinear deformation stage and the total energy curve begins to diverge from the elastic strain energy.

When the stresses get close to the peak strength, the elastic strain energy gradually attains its storage limit. The peak strain energy reflects the capacity of the rock to store the strain energy, i.e., the greater the peak elastic strain energy, the more energy is needed for the rock to fail and consequently higher overall resistance [72, 76]. The peak strain energy is reached at axial strain of 6.84, 6.81, 7.01, and 7.79 ‰, respectively, for rock samples with increasing degree of joint roughness. It is found in Fig. 7 that the peak strain energy of the jointed rock samples increases with the increase in the degree of joint roughness, inferring that an increase in joint roughness enhances the energy storage capacity of the rock. Likewise, during the stages of initiation and coalescence, in contrast to the infinitesimal growth of plastic dissipations for samples with undulating and irregular joint planes, intermittent fluctuations of incremental plastic dissipations occurs in rock samples with smooth and planar joint planes as observed in Fig. 7. This indicates that the dissipated energy is controlled by

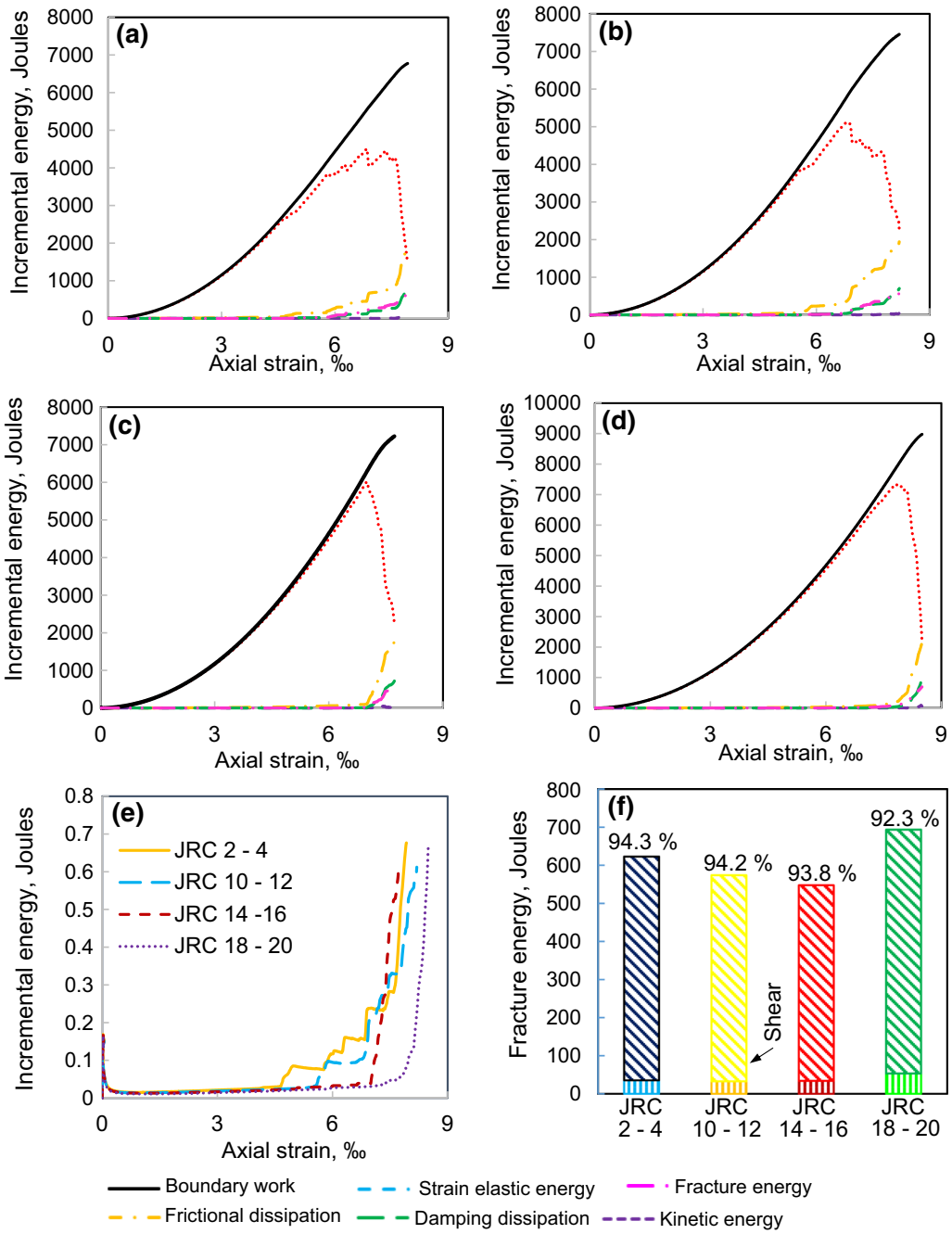

Fig. 7 Evolution of energy in: **a** JRC 2-4; **b** JRC 6-8; **c** JRC 10-12; **d** JRC 14-16; and **e** JRC 18-20 rock samples; **f** incremental fracture energy ratios for the calculated unconfined compression response

the interplay between the competing fracture formation and the frictional sliding properties.

After reaching peak strength, the elastic strain energy is released and the dissipated energy increases rapidly due to the development of macroscopic damage. This can be reflected by the distinct intermittent versus relatively flat increase in plastic dissipation for samples with smooth and rough joint planes by the end of nucleation stage, nevertheless, all samples subsequently follow a sharp increase in incremental energy associated with spikes of microcracking activities during the stage of rupture. It is perceived that, as the degree of joint roughness increases, the amount of input energy due to frictional work, dE_f, decreases accounting for 28%, 26.1%, 24.2%, and 23.9% of the input energy for the cases of JRC 2-4, JRC 10-12, JRC 14-16, and JRC 18-20, respectively.

The results indicate that frictional deformation is a significant term in the energy budget during rock

deformation, with its share of total input energy increasing with the increase in the degree of joint roughness. It also demonstrates that undulating and irregular joint planes provide greater resistance to the frictional sliding of the fractured blocks, which leads to a decline in the relative contribution of the frictional energy to the energy budget as joint surfaces are increasingly roughened.

Additionally, it is revealed that fracture energy (E_{frac}) accounts for a small fraction of the input energy corresponding to 9.2% for JRC 2-4, 7.7% for JRC 10-12, 7.6% for JRC 14-16, and 7.7% for JRC 18-20, respectively. This is consistent with the energy budget estimations based on field data, laboratory, and numerical studies [23, 26, 57]. It is worth noting that only 32.6%, 31.1%, 31.4%, and 32% of all the total microcracks occur in shear mode for rock samples with increasing degree of joint roughness. Nevertheless, the contribution of shear microcracking to total fracture energy released decreased from 94.3% for JRC 2-4, 94.2% for JRC 10-12, 93.8% for JRC 14-16, and 92.3% for JRC 18-20, respectively, as depicted in Fig. 7f.

3.2 Microstructural signatures of fracturing process

The effect of joint roughness on the rock fracture mechanism can be demonstrated using the distributions of acoustic events, contact force network, coordination number, and crack anisotropy. These quantities are considered to be excellent signatures for the propagation of shear rupture.

3.2.1 Spatial distribution of acoustic events and contact force network

Complementing the evolution of contact force networks, the spatial and temporal distribution of microcracks identified by AEs can contribute to a better understanding of the fracture growth mechanisms and their correlation with microstructure. It is well-established that each bond breakage is assumed to be a microcrack in DEM. When a bond breaks, the stored strain energy is released as kinetic energy in the form of a seismic wave. Seismic source information can therefore be calculated for these AEs where microcracks occur close together both in space and time and are considered a single AE event [28, 29]. Figure 8 shows the magnitude and orientation of the contact forces in conjunction with the locations of the associated acoustic emissions for the three deformation stages in samples with increasingly roughened joints. The contact forces are predominantly vertically oriented to counteract the load applied by the uniaxial compressive loading. The diffuse seismicity during the initiation stage is evidence of an essentially spatially uniform stress distribution, which only locally exceeds tensile or shear bond strengths. Toward peak stress, progressive damage is such that fracture interaction and coalescence become increasingly active, leading to an accelerating number of acoustic events with increased size, and culminating in the development of macrofracture.

For rock samples with undulating and irregular joints, the spatial force distribution is quite uniform throughout the sample prior to peak stress, in line with the uniform distribution of event locations. This agrees with the stress–strain relationship (see Fig. 3), which shows that the nucleation and propagation of macrofracture occurs post-peak stress. Simultaneously, during the coalescence stage, samples with smooth and planar joint surfaces gradually exhibit spatially nonuniform forces, of which the crack propagation and coalescence start at the tip of the pre-existing joints and cut through the rock bridges. This leads to AE events that are localized along the joint. Coalescence of event locations to form sharply defined macro-shear planes, just beyond peak stress signifies a strongly focused stress heterogeneity as shown in Fig. 8. The macro-failure planes in the stage of rupture are visible as an absence of soft bond forces (white areas) as these bonds have been broken and cannot reform. The overlapping of AE events indicates that some of the micro cracking activities are, indeed, clustered.

The frequency–magnitude distribution of AE events is used to understand the microcracking mechanisms and damage quantification of rock samples with increasing degree of joint roughness under the uniaxial loading, as shown in Fig. 9. At the peak stress state, the AE magnitudes mainly range from -3.4 to -3 occupying 43.1%, 49.3%, 60%, and 63.4% of the total AE events for the samples with JRC 2-4, 10-12, 14-16, and 18-20, respectively. This increasing trend can be explained considering the fact that external work put into the system is the same for all jointed rock samples. Before the complete formation of macro-fracture surface, if the dissipation of work done by external applied stresses along the joint plane is restrained by surface roughness, the external energy will have to dissipate by developing more cracks within intact matrix resulting in larger quantities of AE events. At the end of the rupture stage, the AE magnitudes mostly range from -3.8 to -3 accounting for 58.2%, 56.9%, 56.9%, 67.4% of the total AE events for these jointed samples, respectively. This can be attributed to the predominant occurrence of smaller post-peak fractures resulting in an increase in the quantities of small events.

To further investigate the progressive damage localization, the Gutenberg-Richter *b-value* is used. The Gutenberg–Richter relationship is expressed as follows:

$$\log N(>M) = a - bM \tag{26}$$

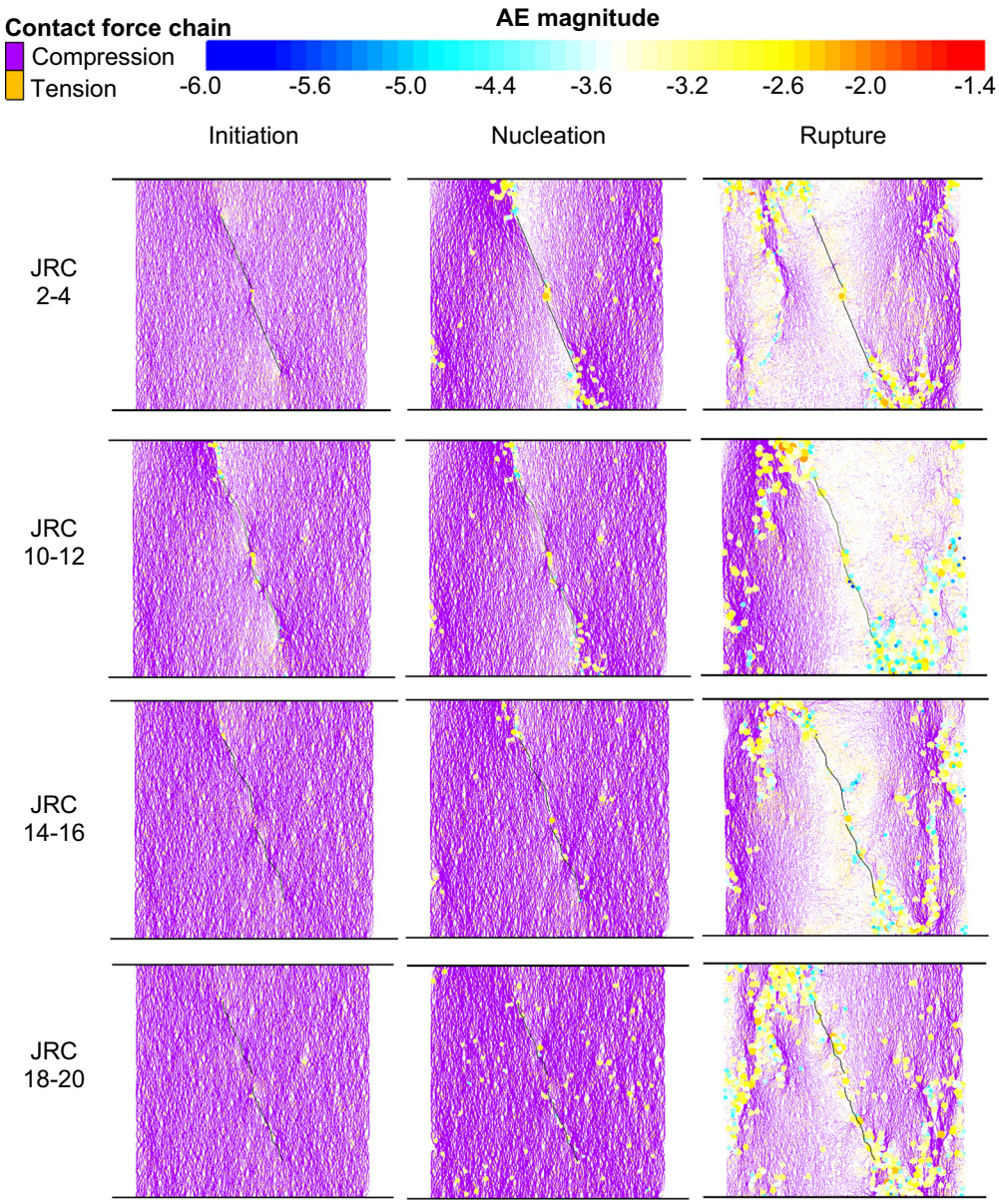

Fig. 8 AE source locations associated with magnitude and force chains in the rock samples under unconfined compression for different degrees of joint roughness. (Note: the color bar indicates the acoustic emission magnitude, *M*, calculated from the kinetic energy of the sources; line thickness indicates force magnitude)

where N is the cumulative number of events with magnitudes larger than M, and a and b are constants. The constant a represents the mean activity level in the local region investigated, while the constant b represents the proportion of frequency of small events in comparison with great events. a large b indicates larger proportion of small events, and vice versa.

Overall, as nucleation and propagation of the macro-fractures occurs post-peak stress, the b values decrease from 1.605 to 1.287, 2.258 to 1.495, 1.871 to 1.511, and 2.324 to 1.548 corresponding to the four rock samples with increasing degree of joint roughness. A reduction in b value implies that a relatively increased number of large-magnitude events occurs, which is evidenced by the range of − 5.4 to − 2.4, − 5.6 to − 2.8, − 5.4 to − 2.6, − 5.4 to − 2.6 increases to − 5.6 to − 2.2, − 6.8 to − 2, − 6.2 to − 2.2, − 6.2 to − 2.2 at the two selected stages for the investigated samples. AE events are mainly composed of no more than 2 and 5 microcracks at the end of coalescence and rupture stages, respectively. The proportions of the events and the corresponding microcracks are summarized in Table 4.

van der Baan and Chorney [55] demonstrated that rock failure dominated by tensile cracking is characterized by a

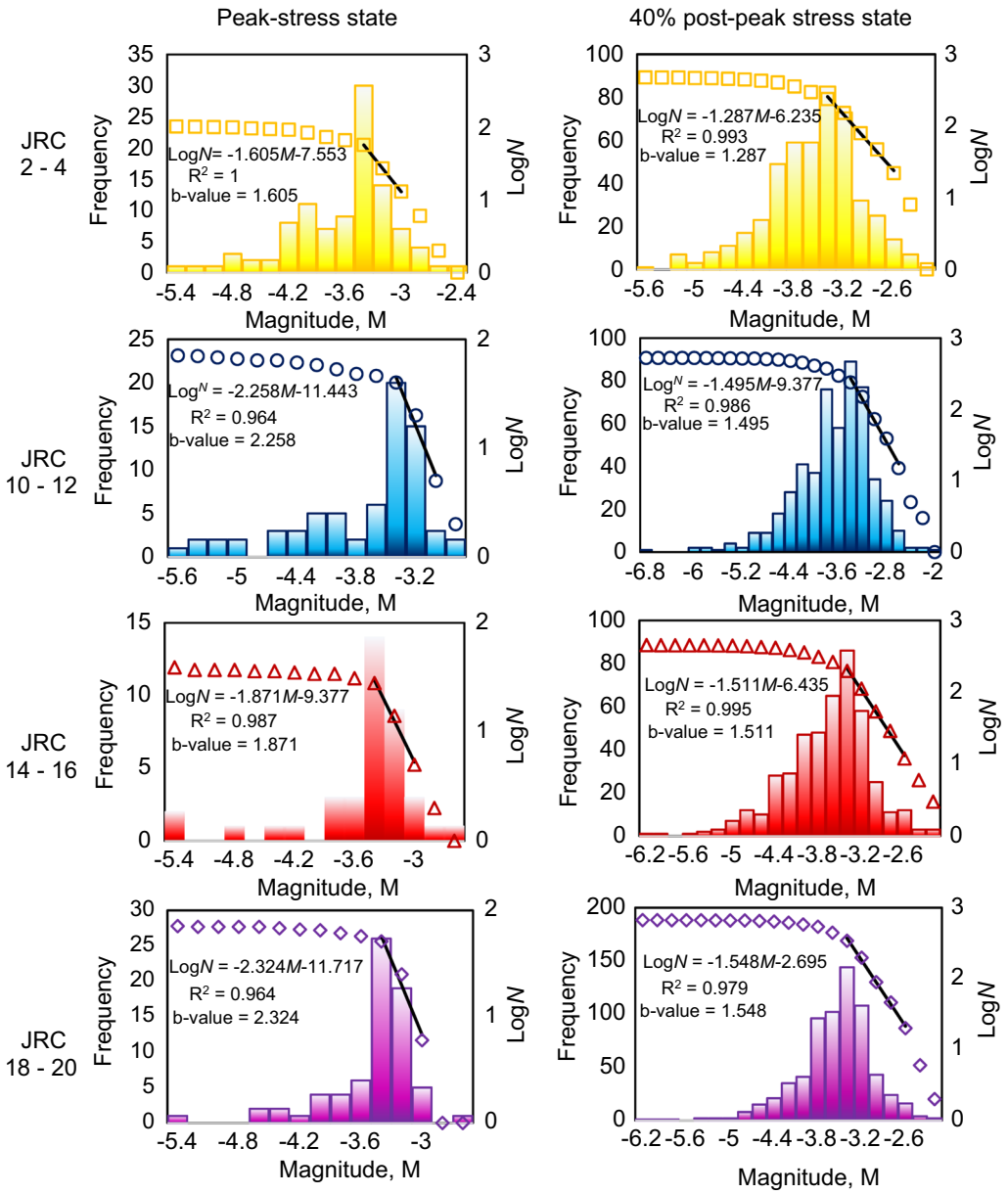

Fig. 9 Distribution of acoustic emission events and estimated *b*-value for different degree of joint roughness

relatively higher number of small-magnitude events, whereas shear-dominated deformation leads to a relatively higher number of large-magnitude events. This coincides well with the above observation of *b* values of 1.287, 1.495, 1.511, and 1.548 with relative ratio of released tensile-to-shear fracture energy of 0.060, 0.061, 0.066, and 0.084, respectively, for the rock samples with JRC 2-4, JRC 10-12, JRC 14-16, and JRC 18-20.

3.2.2 Coordination number

The effects of granular media, having different joint roughness, on the progression of fracture growth and the associated material damage can be expressed using the coordination number, which is calculated using the number of particles (N_p) and their contacts (N_c), as expressed below:

$$C_n = 2\frac{N_c}{N_p} \tag{27}$$

The coordination number (C_n) rises initially as the rock sample compresses, because particles rearrange to achieve greater stability with more contacts as the applied stress increases. Following the rise, C_n values usually decrease owing to the degradation of contacts and bonds and the rock system is free to dilate.

Table 4 Microcracking information and maximum number of cracks for joint roughness

The proportions of the events composed of	JRC 2-4	JRC 10-12	JRC 14-16	JRC 18-20
Peak stress state				
1 microcrack	73.9%	76.5%	64.1%	81.3%
$\leq$ 2 microcracks	85.2%	90.1%	84.6%	96%
The maximum number and corresponding magnitude	7 − 2.6	6 − 3.04	12 − 2.44	4 − 2.57
40% post-peak stress state				
1 microcrack	66.3%	72.1%	69.5%	68.1%
$\leq$ 2 microcracks	79.8%	83.7%	82.5%	83.4%
$\leq$ 5 microcracks	91.7%	94.5%	93.6%	94.7%
The maximum number and corresponding magnitude	41 − 2.78	102 − 1.96	51 − 2.15	29 − 2.53

The results show a systematic trend of bonded particle assembly where increasing the degree of joint roughness results in an increase in coordination number before the peak stress state is reached (see Fig. 10a). This is followed by a decreasing trend in the coordination number after passing the peak stress state. This can be attributed to the fact that highly undulated and irregular joints provide greater resistance to the occurrence of slippage along the weak planes, which delays the onset of failure. Contrarily, for the case of rock samples with low values of JRC, the evolution of coordination number, considering all contacts, is essentially intermittent. This indicates the presence of an interplay between competing processes involving the nucleation and localization of shear and conjugate fractures, in addition to the frictional movements of particles along the smooth and planar joints. This is consistent with the macroscopic deformation behavior reflected by the irregular drops in axial stress (Fig. 3).

As illustrated in Fig. 10b, the bulk volumetric changes of the jointed rock sample are closely related to the tendency of a particulate assemblage to dilate or contract. This can be attributed to the fact that dilatancy is increasingly suppressed in samples that are embedded within more pronounced rough joints. The undulated and irregular joints are found to facilitate further interlocking of the connected grain contacts that can strengthen the mechanical stability of the rock.

As depicted in Fig. 10c, the coordination number of soft bonds is relatively constant at the elastic deformation stage and starts to decrease when the axial strain reaches 4.67, 5.71, 7.06, and 7.39 ‰ for JRC 2-4, JRC 10-12, JRC 14-16, and JRC 18-20, respectively. This observation is in conformity with the rock fracturing behavior, at which significant increments of microcracks and increasing number of debonded particles start to develop. In addition, the coordination number of the soft bonds exhibits apparent decreasing trends with more distinct decrease for the cases rock samples embedded with undulating and irregular joints (see Fig. 10c). This is explained by the asperities of large amplitudes and inclination angles that contribute to the localization and rapid coalescence of microcracks. Simultaneously, the fracture mass density (P_{21}), defined as the total fracture length per unit area, records a shift from intermittent to abrupt rise in damage accumulation with the increase in the degree of joint roughness as shown in Fig. 10d. Overall, when a spike in bond breakage activity develops as compression proceeds, the corresponding propagation and clustering of microcracks can be identified by a drop in the coordination number, which indicates shear-band formation. These observations are consistent with those made by Asadizadeh et al. [3] based on experimental results.

3.2.3 Crack anisotropy and crack tensor

To characterize the progression of fracture growth and the associated material damage, the crack tensor, that describes the density of broken bonds and crack normal, is utilized. The crack tensor allows for the microcracking distribution to be quantified with respect to the direction of crack normal [16]:

$$R_{ij} = \frac{1}{A}\sum_{k=1}^{N}\left[(d^2)n_i n_j\right]_k \tag{28}$$

where d is the average diameter of the two adjoining disks, n_i and n_j are the i th and j th components of the crack normal vector, respectively, for a crack k,N is the total crack number, and A is the sample area.

The first (isotropic) invariant of the crack tensor represents the overall magnitude of damage, while the second (deviatoric) invariant indicates the anisotropy of damage.

The first invariant of the crack tensor determines the crack intensity or crack density:

$$\chi_d = (R_{11} + R_{22}) = \frac{1}{A}\sum d^2 \tag{29}$$

where $d = 2r$ is the crack length.

Crack density is a scalar and isotropic parameter that does not convey information about the anisotropy of crack formation under the UCS loading. The crack anisotropy can be characterized by the second invariant of the tensor:

$$\alpha = \frac{4}{\chi_d}\sqrt{\frac{1}{4}(R_{11} - R_{22})^2 + R_{12}^2} \tag{30}$$

The crack tensor can alternatively be expressed as:

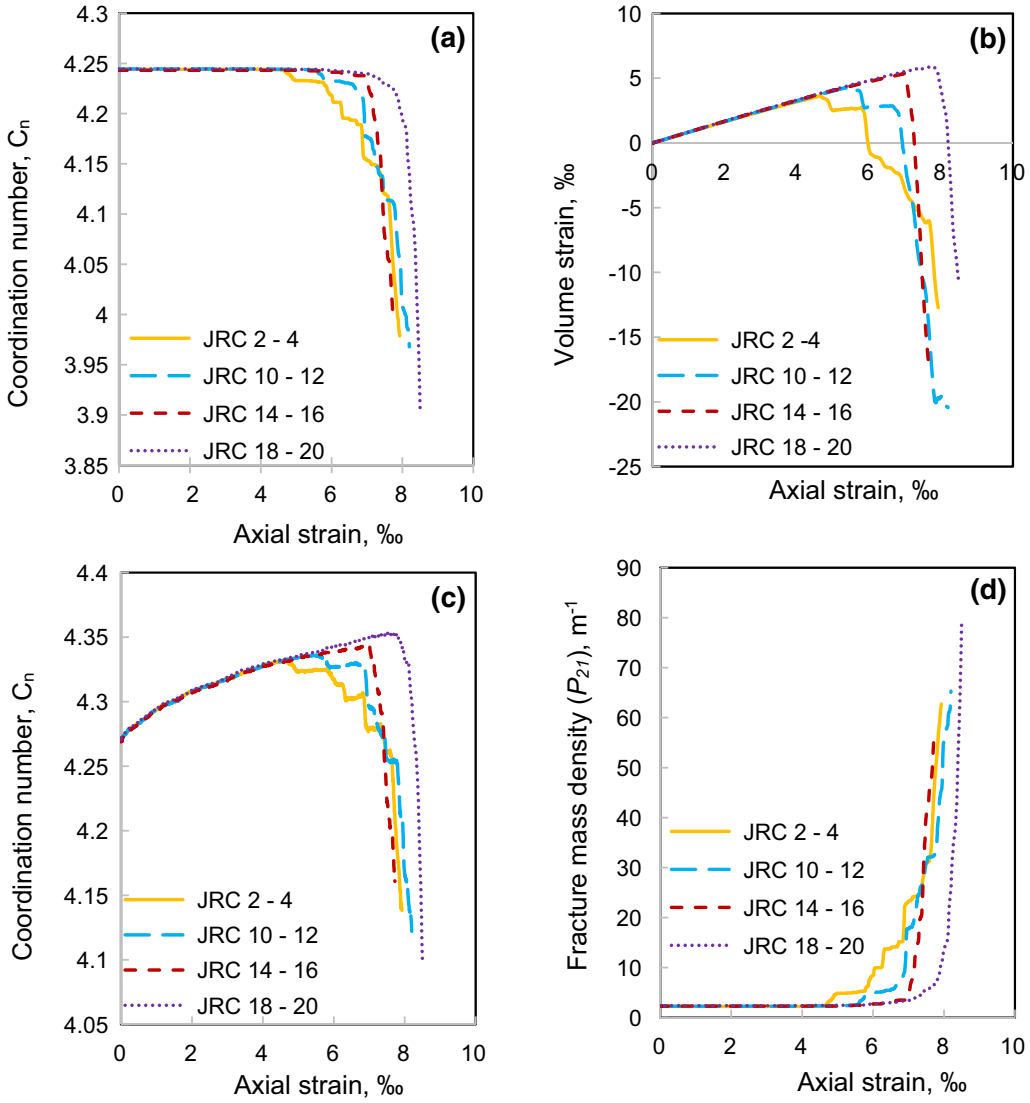

Fig. 10 Effects of joint roughness **a** on coordination number considering all engaged contacts; **b** on volumetric changes; **c** on coordination number considering all bonded contacts; **d** on fracture mass density

$$R_{ij}n_in_j = \frac{\chi}{2}(1 + \alpha\cos 2(\theta - \theta_0)) \tag{31}$$

Taking the data set of crack normal orientations each vector is binned into an angular interval $\Delta\theta$ centered around an angle θ. The number of cracks in each bin is given by $\Delta\chi(\theta)$ and is normalized by the product $\chi\Delta\theta$, where χ is the crack density. Then, the probability distribution function, $S(\theta)$, of the crack normal orientations can be expressed as:

$$S(\theta) = \frac{\Delta\chi(\theta)}{\chi\Delta\theta} \tag{32}$$

A second-order Fourier approximation is employed to characterize the probability distribution function, $S(\theta)$, of the crack normal orientations:

$$S(\theta) = \frac{1}{2\pi}(1 + \alpha\cos 2(\theta - \theta_0)) \tag{33}$$

where θ_0 is the orientation of the major principal anisotropy; and α is the coefficient of anisotropy. For a completely isotropic distribution of cracks, $\alpha = 0$; for an array of mutually parallel cracks $\alpha = 1$.

As shown in Fig. 11a, first (isotropic) invariant of the crack tensor, representative of crack intensity by dint of reflecting the overall magnitude of damage, increases with the increase in the degree of joint roughness and follows a pattern consistent with the cumulative number of microcracks. With the increase in joint roughness, the evolution of the first (isotropic) invariant of the crack tensor χ_d gradually transits from an intermittent increase to a significant surge. As fracture growth progresses from initiation to

rupture, a significant decline in the second invariant of the crack tensor, symbolic of crack anisotropy, is illustrated in Fig. 11b. This can be attributed to the fact that the coalescence of pre-existing joints and smaller fractures, assisted by newly generated microcracks, is able to form of a through-going shear rupture in a specific direction. This is in contrast to the uniformly distributed microcracks that develop in the stage of initiation. Noteworthy is the crack anisotropy in JRC 14-16 rock sample is pronouncedly larger than that of others within the axial strain range from 5.7 to 7.1‰, corresponding approximately to the Stage II (nucleation). During this stage, more microcracks are generated in the rock samples other than that of JRC 14-16, which can be further reinforced from the observation in Fig. 3. Consequently, larger quantities of microfractures are more likely to coalesce and nucleate, which can cause the emergent fracture networks to be more connected and thereby less anisotropic.

To better understand the crack anisotropy, the crack normal distributions are presented using polar histograms as shown in Fig. 12. The polar histograms are obtained by statistically collecting the microcracking orientation at angular interval (bin angle) of 10°. In addition, the Fourier Series Approximations (FSA) are applied herein as a quantitative measure for crack anisotropy. The basic idea is that the orientation can be described using a probability density function such that the crack normal distribution function, $S(\theta)$, provides the portion of microcracking orientation that fall within the bin angle. It can be seen in Fig. 12 that the values of the coefficient of anisotropy,α, are revolving around 0.6, indicating that the generated microfracture distributions in these investigated rock samples bear a very close resemblance as a result of the same loading direction and major orientation as well as the length of the per-existing joints. The subtle difference is attributed to joint morphology that is characterized by different levels of undulation of waviness with various amplitudes and inclination angles. In addition, the privileged directions of crack normal in all investigated samples tend to coincide with the major principal stress direction, because it is favored in the occurrence of bond breakages during the course of uniaxial compression.

3.3 Impact of joint orientation

To investigate the impact of joint orientation on the mechanical behavior of the rock samples with increasing degree of joint roughness, joint angle β is varied from 0° (horizontal joints) to 90° (vertical joints) with an interval of 22.5°. The effect of joint angle on the uniaxial compressive strength (σ_{ucs}) and rock mass deformation modulus E_m is shown in Fig. 13. The highest values of σ_{ucs} and E_m are

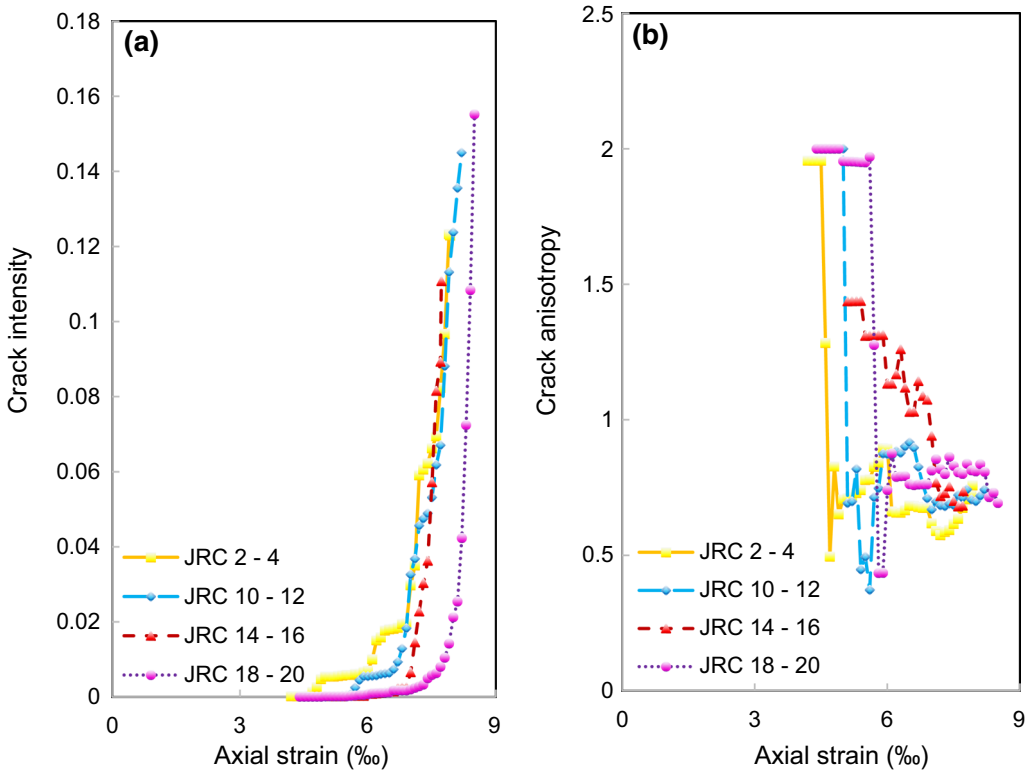

Fig. 11 Evolution of **a** crack intensity and **b** crack anisotropy as a function of cumulative axial strain in jointed rock samples with increasing joint roughness

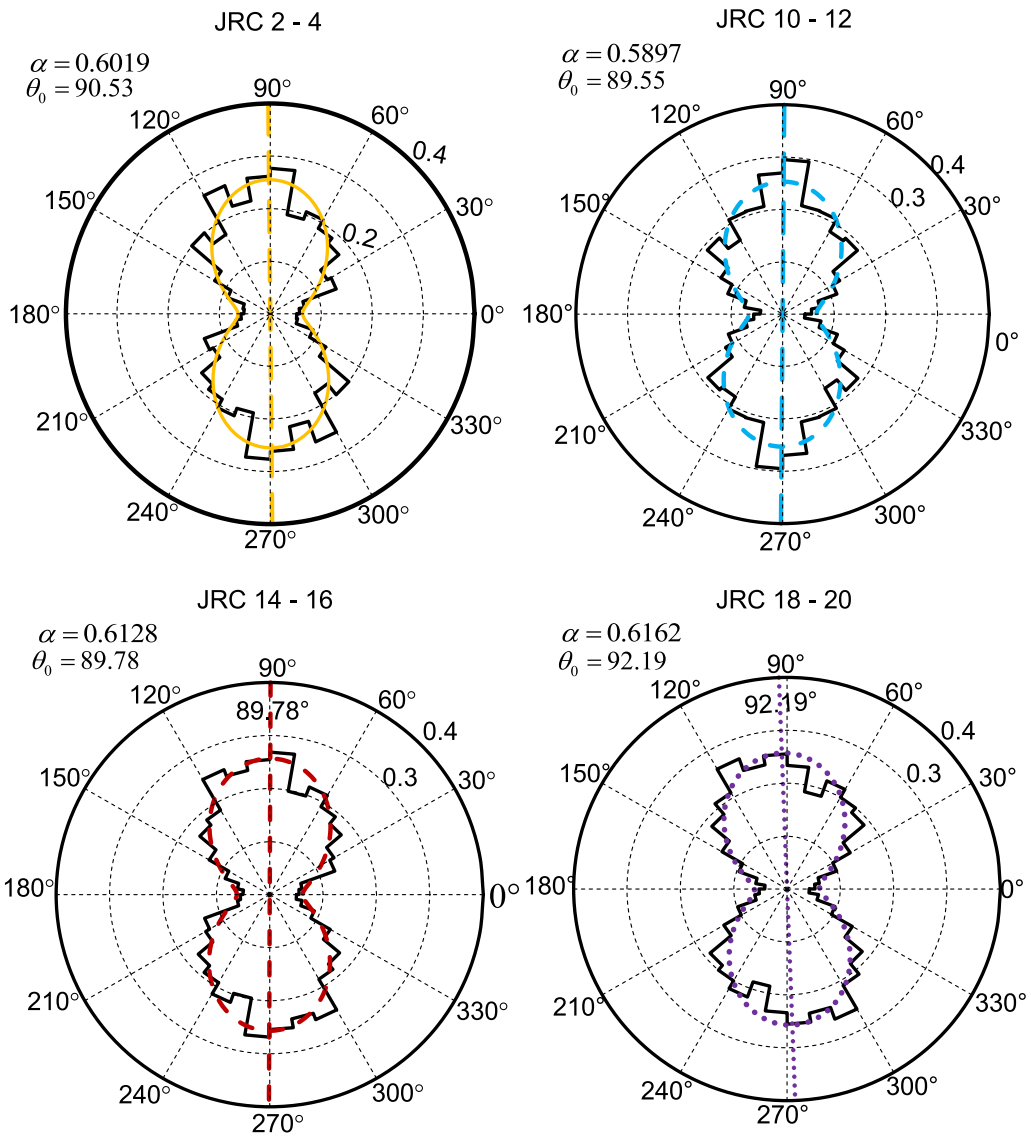

Fig. 12 Effect of degree of joint roughness on the distribution microcracking normals and the associated tensor approximation

found when β is 0° for the four investigated samples. The values of σ_{ucs} and E_m for all samples then exhibit a decreasing trend, and the lowest values are found for the case of β = 67.5° before rebounding to relatively higher values at β = 90°.

To understand the mechanical behavior and fracturing process in response to the changes of joint orientations, visual representation of microcrack locations for the case of JRC 18-20 is shown in Fig. 14a. Fracture patterns obtained from the analysis are generally in good agreement with the observations made by Asadizadeh et al. [3], indicating that the soft-bonded particle model is able to capture the deformation process and the failure mechanism of the investigated rock samples. At inclination angles of 0° and 22.5°, microcracks predominantly occur in intact rock matrix and merge into a macroscopic fracture, in particular, the generated macrofailure plane in the rock sample at β = 0° matches what is observed in laboratory experiment of Asadizadeh et al. [3]. As a comparison, when the β increases to 45° and 67.5°, interaction and

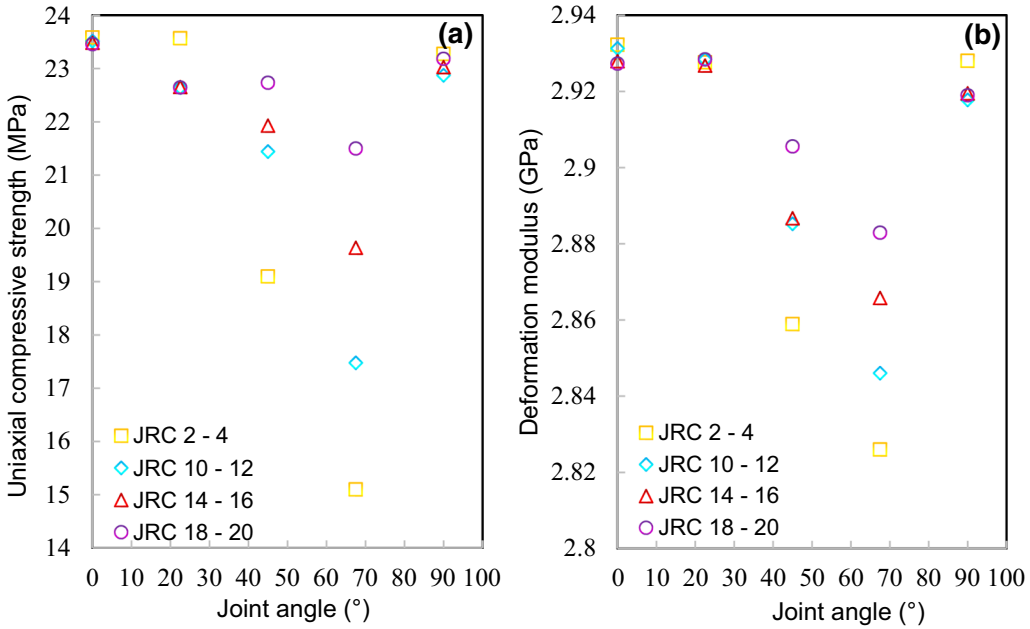

Fig. 13 Effect of joint orientation angle on: **a** the uniaxial compressive strength; **b** the deformation modulus

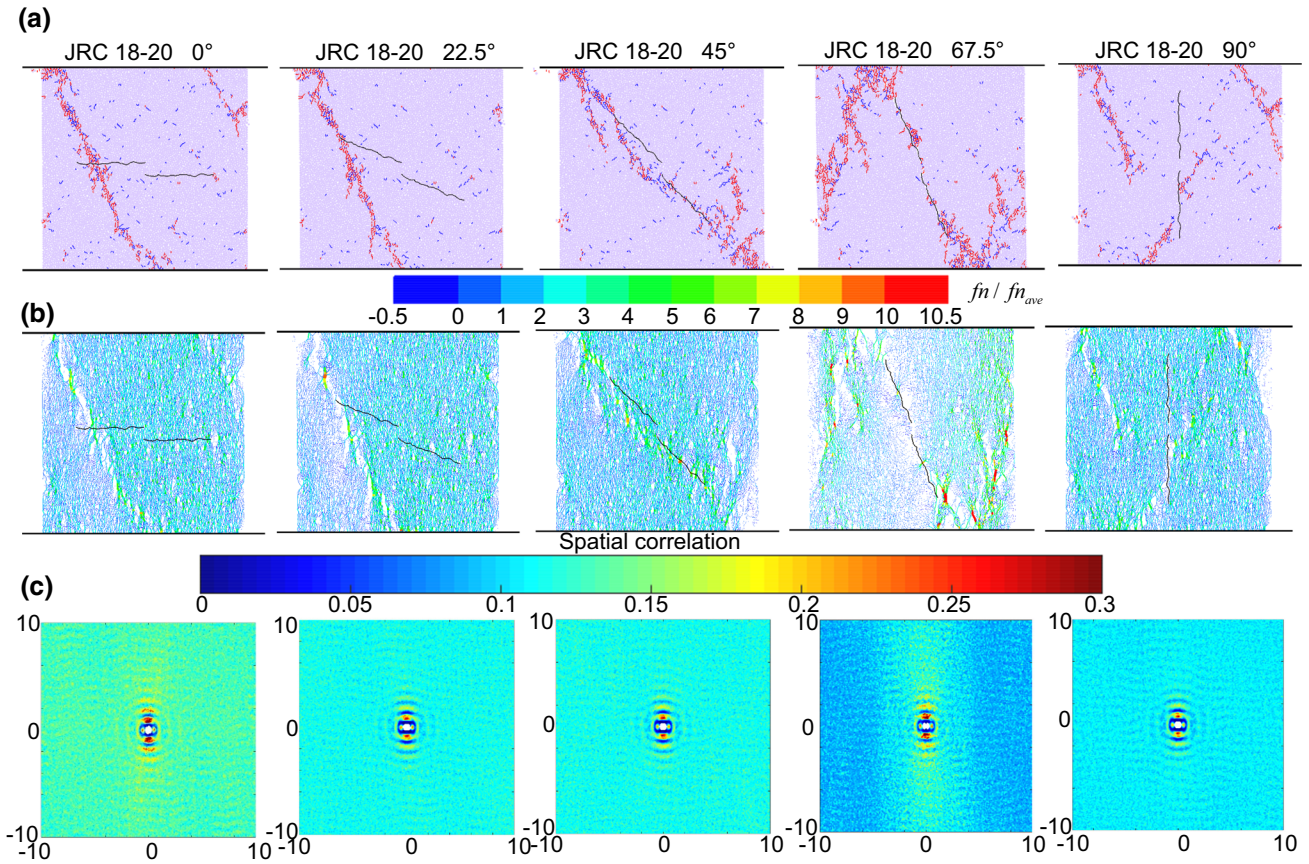

Fig. 14 **a** Microcrack distribution within the jointed rock samples; **b** distribution of contact normal forces; **c** spatial correlation distribution of the contact normal

coalescence of joint planes and microcracks form sharply defined macroshear planes that clearly display the complex failure mode. Although failure develop mostly within intact rock, it is largely influenced by the pre-existing joints and the interlocking of blocks. At $\beta = 90°$, new microcracks and fractures fail to develop and merge to form a through-going shear rupture. Only crushing failure at the sample-platen interfaces and smaller shear fracture enveloped by tensile microcracks are observed. This reflects why the deformability and strength first exhibit a decreasing trend and then rebound. The calculated failure mechanism is in line with the experimental work of Walton et al. [58], and other bonded particle analysis that focus on the role of joint orientation on the rock deformation [46, 47, 62, 77].

Computing the 2D spatial correlation function $G(r)$ of the normal contact forces acting on the particles can provide new insights into the effect of the joint orientation angle on the mechanical response of jointed rock samples under uniaxial compressive loadings. $G(r)$ is defined the same manner as reported by Løvoll et al. [40]:

$$G(r) = \frac{\sum_{i=1}^{N} \sum_{j>i} \delta\left(|r_{ij} - r|\right) f_i f_j}{\sum_{i=1}^{N} \sum_{j>i} \delta(|r_{ij} - r|)} \tag{34}$$

where N is the total number of contact points, f_i is the normalized normal contact force acting at contact i, r_{ij} is the distance between contacts i and j, and $\delta(0) = 1$. A force pair is two normal forces f_i and f_j separated by r_{ij} which together contribute to the spatial correlation function. A nonzero value of $G(r)$ indicates that, on average, two contacts separated by a distance r have forces that are correlated [22, 41].

The correlation demonstrates that two particles at distance r are connected through a cluster of simultaneously contacting particles, and the force of one particle is transmitted through the network to the other particle [39]. Figure 15 illustrates the correlations of normal contact force for JRC 18-20 rock samples with increasing joint angle at the final damage stage. Note that the radial distance has been normalized with respect to the mean particle diameter d_{50}. Apparently, $G(r)$ has higher peaks before r reaches $4d_{50}$, representative of the higher interparticle locking. The amplitude of oscillation is found to decrease with the increase in radial distance. At a distance greater than four times the mean particle diameter, slight oscillation around unity is observed. In addition, the local correlation between contact points indicates that macroscopic fractures take place mostly within intact rock matrix. This is confirmed by the tightly connected distribution of contact points in the system as a result of the fewer microcracking that have been generated.

To understand the effect of joint orientation on the deformability and fracture growth of these jointed rock

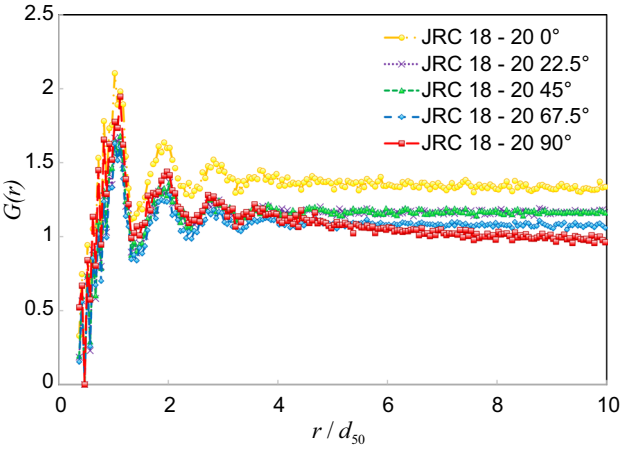

Fig. 15 Effect of joint orientation angle on the changes in spatial force correlation function $G(r)$ with distance for jointed rock with JRC 18-20

samples, Fig. 14 presents the micro-scale characterization of the normal contact force distribution and the corresponding spatial correlation map. Associated with the clustering of microcracks and fractures in the intact matrix, contact forces are distributed more uniformly in the samples when β is 0°, 22.5°, and 90°. This is further illustrated by the strong spatial correlation of contact forces as presented in Fig. 14c. In contrast, the inhomogeneity of the force chains is localized around the joint planes in samples with intermediate inclination angles of 45° and 67.5° that reveals the increasingly dominant role of joint surface in the failure mechanism (see Fig. 14b). In particular, the absence of contact forces indicates the coalescence of microcracks into a through-going shear rupture, which result in the relatively weaker spatial correlation between forces.

3.4 Limitations and future outlook

It is recognized that actual joint morphology cannot be fully described using the well-known standard joint roughness profiles proposed by Barton and Choubey [7] because of the complexity of natural joint surfaces. However, the proposed joint roughness coefficient (JRC) as well as the standard JRC profiles can integrate quantitative and qualitative descriptions to identify the characteristic joint surface roughness in relation to the deformability and mechanical strength of a rock mass [5, 19, 31]. Moreover, the approach has been recommended by ISRM [6] and has been widely used in engineering practices. Thus, not only is this study examines the effect of joint roughness on the rock strength and mechanical behavior of the rock material but also provides new insights into the micromechanical nature of the deformability and fracture development in rough-jointed rock samples under unconfined compression.

Notwithstanding these promising results, future research into the irregularity and randomness of natural structural planes should be considered to advance our understanding of the natural rock topography and correlate the response with laboratory values.

4 Conclusions

The deformation and failure process of rock samples that have non-persistent rough joints have been numerically investigated using unconfined compression tests. Smooth-joint contact and soft bond models are selected to represent the pre-existing joints and the rock matrix, respectively. The progressive damage is visually represented. The mechanical response and cracking behavior of the samples are found to be in agreement with experimental results. The results show that strength and deformability of the jointed rocks are highly dependent on the joint roughness and orientation. The following conclusions can be drawn from the numerical analysis:

1. As fracture growth progresses from initiation to rupture, the transition of microcrack distribution and spatial location of AE from being diffused to strongly localized is evidenced by the decrease in the Gutenberg–Richter *b*-value. This is usually associated with macro-rupture of the rock samples and the development of spatially nonuniform stress heterogeneity.
2. As the degree of joint roughness increases, the peak strain energy of the jointed rock samples increases, which enhances the energy storage capacity of the rock.
3. AE source locations are largely affected by the joint morphology. Compared to smooth and planar joints, the undulated and irregular joint planes are favorable for the localization and clustering of acoustic emissions.
4. The abrupt spike of the first and the sudden drop of the second invariants of the crack tensor indicates a change from random to localized damage accumulation pattern, which confirms the formation of shear and conjugate fractures within the jointed rock samples.
5. The distribution and spatial correlation of contact forces with the corresponding density map provide micromechanical insights into the role of joint inclination angles on the strength and deformation behavior of jointed rock.

Acknowledgement This research is supported by a research grant from the Natural Sciences and Engineering Research Council of Canada and the Shanghai Sailing Program (21YF1419200). The first author is thankful to Prof. Mostafa Asadizadeh of Hamedan University of Technology for generously sharing the experimental data.

References

1. Alejano LR, Arzúa J, Bozorgzadeh N, Harrison JP (2017) Triaxial strength and deformability of intact and increasingly jointed granite samples. Int J Rock Mech Min Sci 95:87–103
2. Asadizadeh M, Hossaini MF, Moosavi M, Masoumi H (2018) Shear strength and cracking process of non-persistent jointed rocks: an extensive experimental investigation. Rock Mech Rock Eng 51:415–428
3. Asadizadeh M, Hossaini MF, Moosavi M, Masoumi H, Ranjith PG (2019) Mechanical characterisation of jointed rock-like material with non-persistent rough joints subjected to uniaxial compression. Eng Geol 260:105224
4. Bahaaddini M, Sharrock G, Hebblewhite BK (2013) Numerical investigation of the effect of joint geometrical parameters on the mechanical properties of a non-persistent jointed rock mass under uniaxial compression. Comput Geotech 49:206–225
5. Bahaaddini M, Hagan PC, Mitra R, Hebblewhite BK (2014) Scale effect on the shear behaviour of rock joints based on a numerical study. Eng Geol 181:212–223
6. Brown ET (1981) Rock characterization testing and monitoring-ISRM suggested methods. Pergamon Press, Oxford, p 211
7. Barton N, Choubey V (1977) The shear strength of rock joints in theory and practice. Rock Mech Rock Eng 10(1):1–54
8. Brace WF, Bombolakis EG (1963) A note on brittle crack growth in compression. J geophys Res 68:3709–3713
9. Camones LAM, Vargas EDA, de Figueiredo RP, Velloso RQ (2013) Application of the discrete element method for modeling of rock crack propagation and coalescence in the step-path failure mechanism. Eng Geol 153:80–94
10. Chiu CC, Wang TT, Weng MC, Huang TH (2013) Modeling the anisotropic behavior of jointed rock mass using a modified smooth-joint model. Int J Rock Mech Min Sci 62:14–22
11. Cho N, Martin CD, Sego DC (2007) A clumped particle model for rock. Int J Rock Mech Min Sci 44(7):997–1010
12. Cundall P, Hart R (1992) Numerical modeling of discontinua. Eng Comput 2:101–113
13. Cundall PA, Strack ODL (1979) A discrete element model for granular assemblies. Geotéchnique 29(1):47–65
14. Desbois G, Höhne N, Urai JL, Bésuelle P, Viggiani G (2017) Deformation in cemented mudrock (Callovo-Oxfordian Clay) by microcracking, granular flow and phyllosilicate plasticity: insights from triaxial deformation, broad ion beam polishing and scanning electron microscopy. Solid Earth 8:291–305
15. De Silva VRS, Ranjith PG (2020) A study of rock joint influence on rock fracturing using a static fracture stimulation method. J Mech Phys Solids 137:103817
16. Diederichs MS (1999) Instability of hard rockmasses: the role of tensile damage and relaxation. PhD thesis. Department of Civil Engineering, University of Waterloo, Waterloo
17. Dinç O, Scholtès L (2018) Discrete analysis of damage and shear banding in argillaceous rocks. Rock Mech Rock Eng 51:1521–1538
18. Duan K, Kwok CY, Ma X (2017) DEM simulations of sandstone under true triaxial compressive tests. Acta Geotech 12:495–510
19. Fardin N, Stephansson O, Jing L (2001) The scale dependence of rock joint surface roughness. Int J Rock Mech Min Sci 38:659–669
20. Feng P, Xu Y, Dai F (2021) Effects of dynamic strain rate on the energy dissipation and fragment characteristics of cross-fissured rocks. Int J Rock Mech Min Sci 138:1
21. Gao G, Meguid MA, Chouinard LE, Xu C (2020) Insights into the transport and fragmentation characteristics of earthquake-induced rock avalanche: A numerical study. ASCE Int J Geomech 20(9):1–23

22. Gao G, Meguid MA, Chouinard LE (2020) On the role of pre-existing discontinuities on the micromechanical behavior of confined rock samples: a numerical study. Acta Geotech 15:3483–3510
23. Gao G, Meguid MA, Chouinard LE, Zhan WW (2021) Dynamic disintegration processes accompanying transport of an earthquake-induced landslide. Landslides 18(3):909–933
24. Garcia FE, Bray JD (2018) Distinct element simulations of earthquake fault rupture through materials of varying density. Soils Found 58(4):986–1000
25. Ge Y, Kulatilake PHSW, Tang H, Xiong C (2014) Investigation of natural rock joint roughness. Comput Geotech 55:290–305
26. Goodfellow SD, Nasseri MHB, Maxwell SC, Young RP (2015) Hydraulic fracture energy budget: insights from the laboratory. Geophys Res Letters 42:3179–3187
27. Haeri H, Shahriar K, Marji MF, Moarefvand P (2014) Experimental and numerical study of crack propagation and coalescence in pre-cracked rock-like disks. Int J Rock Mech Min Sci 67:20–28
28. Hazzard JF, Young RP (2000) Simulating acoustic emissions in bonded-particle models of rock. Int J Rock Mech Min Sci 37(5):867–872
29. Hazzard JF, Young RP, Maxwell SC (2000) Micromechanical modeling of cracking and failure in brittle rocks. J Geophys Res 105:16683–16697
30. Huang F, Shen J, Cai M, Xu CS (2019) An empirical UCS model for anisotropic blocky rock masses. Rock Mech Rock Eng 52:3119
31. Huang SK, Oelfke SM, Speck RC (1992) Applicability of fractal characterization and modelling to rock joint profiles. Int J Rock Mech Min Sci Geomech Abstr 29(2):89–98
32. Huillca Y, Silva M, Ovalle C, Quezada JC, Carrasco S, Villavicencio GE (2021) Modelling size effect on rock aggregates strength using a DEM bonded-cell model. Acta Geotech 16:699–709
33. Itasca Consulting Group, Inc. (2019) PFC—particle flow code in 2 and 3 dimensions, version 6.0. Documentation Set of version 6.00.17. Itasca, Minneapolis
34. Jiang M, Shen Z, Wang J (2015) A novel three-dimensional contact model for granulates incorporating rolling and twisting resistances. Comput Geotech 65:147–163
35. Jing L (2003) A review of techniques, advances and outstanding issues in numerical modelling for rock mechanics and rock engineering. Int J Rock Mech Min Sci 40(3):283–353
36. Khazaei C, Hazzard J, Chalaturnyk R (2016) A discrete element model to link the microseismic energies recorded in caprock to geomechanics. Acta Geotech 11(6):1351–1367
37. Li K, Yin ZY, Cheng Y, Cao P, Meng J (2020) Three-dimensional discrete element simulation of indirect tensile behaviour of a transversely isotropic rock. Int J Numer Anal Meth Geomech 44(13):1812–1832
38. Li XF, Li HB, Zhao J (2019) The role of transgranular capability in grain-based modelling of crystalline rocks. Comput Geotech 110:161–183
39. Lois G, Lemaître A, Carlson J (2007) Spatial force correlations in granular shear flow. I. Numerical evidence. Phys Rev E 76(2):021302
40. Løvoll G, Måløy KJ, Flekkøy EG (1999) Force measurements on static granular materials. Phys Rev E 60(5):5872
41. Ma G, Regueiro RA, Zhou W, Liu J (2018) Spatiotemporal analysis of strain localization in dense granular materials. Acta Geotech 14(4):973–990
42. Ma Y, Huang H (2018) DEM Analysis of Failure Mechanisms in the Intact Brazilian Test. Int J Rock Mech Min Sci 102:109–119
43. Ma Y, Huang H (2021) Effect of shear bond failure on the strength ratio in DEM modeling of quasi-brittle materials. Acta Geotech 16:2629–2642
44. Mohd-Nordin MM, Song KI, Cho GC, Mohamed Z (2014) Long-wavelength elastic wave propagation across naturally fractured rock masses. Rock Mech Rock Eng 47(2):561–573
45. Park CH, Bobet A (2009) Crack coalescence in specimens with open and closed flaws: a comparison. Int J Rock Mech Min Sci 46:819–829
46. Park B, Min KB (2015) Bonded-particle discrete element modeling of mechanical behavior of transversely isotropic rock. Int J Rock Mech Min Sci 76:243–255
47. Park B, Min KB, Thompson N, Horsrud P (2018) Three-dimensional bonded-particle discrete element modeling of mechanical behavior of transversely isotropic rock. Int J Rock Mech Min Sci 110:120–132
48. Patel S, Martin CD (2020) Impact of the initial crack volume on the intact behavior of a bonded particle model. Comput Geotech 127:103764
49. Potyondy DO, Cundall PA (2004) A bonded-particle model for rock. Int J Rock Mech Mining Sci 41(8):1329–1364
50. Quiñones J, Arzúa J, Alejano LR, García-Bastante F, Mas Ivars D, Walton G (2017) Analysis of size effects on the geomechanical parameters of intact granite samples under unconfined conditions. Acta Geotech 12:1229–1242
51. Reyes O, Einstein HH (1991) Failure mechanisms of fractured rock: a fracture coalescence model. In: 7th ISRM congress, Aachen, pp 333–340
52. Scholtès L, Donzé FV, Khanal M (2011) Scale effects on strength of geomaterials, case study: coal. J Mech Phys Solids 59(5):1131–1146
53. Scholtès L, Donzé FV (2013) A DEM model for soft and hard rocks: role of grain interlocking on strength. J Mech Phys Solids 61:352–369
54. Shang J, West LJ, Hencher SR, Zhao Z (2018) Tensile strength of larger-scale incipient rock joints: a laboratory investigation. Acta Geotech 13:869–886
55. van der Baan M, Chorney D (2019) Insights from micromechanical modeling of intact rock failure: event characteristics, stress drops and force networks. J Geophys Res Solid Earth 124:12955–12980
56. Varela Valdez A, Morel S, Marache A, Hinojosa M, Riss J (2018) Influence of fracture roughness and micro-fracturing on the mechanical response of rock joints: a discrete element approach. Int J Fract 213:87–105
57. Vora HB, Morgan JK (2019) Microscale characterization of fracture growth and associated energy in granite and sandstone analogs: insights using the discrete element method. J Geophys Res Solid Earth 124:7993–8012
58. Walton G, Alejano LR, Arzua J, Markley T (2018) Crack damage parameters and dilatancy of artificially jointed granite samples under triaxial compression. Rock Mech Rock Eng 51:1637–1656
59. Wong LNY, Li HQ (2013) Numerical study on coalescence of two coplanar pre-existing flaws in rock. Int J Solids Struct 50:3685–3706
60. Wong RHC, Chau KT (1998) Crack coalescence in a rock-like material containing two cracks. Int J Rock Mech Min Sci Geomech Abst 35:147–164
61. Wu H, Guo N, Zhao J (2018) Multiscale modeling and analysis of compaction bands in high-porosity sandstones. Acta Geotech 13(3):575–599
62. Xu GW, He C, Chen ZQ, Wu D (2018) Effects of the microstructure and micro-parameters on the mechanical behaviour of transversely isotropic rock in Brazilian tests. Acta Geotech 13:887–910

63. Xu G, Hu X, Tang R (2021) Fracture evolution of transversely isotropic rocks with a pre-existing flaw under compression tests based on moment tensor analysis. Acta Geotech. https://doi.org/10.1007/s11440-021-01214-9
64. Xu G, Gutierrez M, He C (2021) Modeling of the effects of weakness planes in rock masses on the stability of tunnels using an equivalent continuum and damage model. Acta Geotech 16:2143–2164
65. Xu G, Gutierrez M, He C, Meng W (2020) Discrete element modeling of transversely isotropic rocks with non-continuous planar fabrics under Brazilian test. Acta Geotech 15:2277–2304
66. Xu X, Wu S, Gao Y (2016) Effects of micro-structure and micro-parameters on brazilian tensile strength using flat-joint model. Rock Mech Rock Eng 49:3575–3595
67. Yang SQ, Jing HW (2011) Strength failure and crack coalescence behavior of brittle sandstone samples containing a single fissure under uniaxial compression. Int J Fract 168:227–250
68. Yang XX, Kulatilake PHSW, Chen X, Jing HW, Yang SQ (2016) Particle flow modeling of rock blocks with nonpersistent open joints under uniaxial compression. ASCE Int J Geomech 16(6):04016020
69. Zhao C, Zhou YM, Cf Z (2018) Cracking processes and coalescence modes in rock-like specimens with two parallel pre-existing cracks. Rock Mech Rock Eng 51:3377–3393
70. Zhao T, Liu Y (2020) A novel random discrete element analysis of rock fragmentation. Int J Numer Anal Meth Geomech 44(10):1386–1395
71. Zhao Y, Semnani SJ, Yin Q, Borja RI (2018) On the strength of transversely isotropic rocks. Int J Numer Anal Methods Geomech 42:1917–1934
72. Zhang LM, Cong Y, Meng FZ, Wang ZQ, Zhang P, Gao S (2021) Energy evolution analysis and failure criteria for rock under different stress paths. Acta Geotech 16:569–580
73. Zhang SH, Wu SC, Duan K (2019) Study on the deformation and strength characteristics of hard rock under true triaxial stress state using bonded-particle model. Comput Geotech 112:1–16
74. Zhang XP, Wong LNY (2013) Crack initiation, propagation and coalescence in rock-like material containing two flaws: a numerical study based on bonded-particle model approach. Rock Mech Rock Eng 46:1001–1021
75. Zhang XP, Zhang Q, Wu SC (2017) Acoustic emission characteristics of the rock-like material containing a single flaw under different compressive loading rates. Comput Geotech 83:83–97
76. Zhang Y, Feng XT, Zhang XW, Wang ZF, Sharifzadeh M, Yang CX (2019) A novel application of strain energy for fracturing process analysis of hard rock under true triaxial compression. Rock Mech Rock Eng 52(2):1–16
77. Zhou C, Xu C, Karakus M, Shen J (2019) A particle mechanics approach for the dynamic strength model of the jointed rock mass considering the joint orientation. Int J Numer Anal Methods Geomech 43:2797–2815
78. Zhou W, Ji X, Ma G, Chen Y (2020) FDEM simulation of rocks with microstructure generated by Voronoi grain-based model with particle growth. Rock Mech Rock Eng 53(4):1909–1921

Publisher's Note Springer Nature remains neutral with regard to jurisdictional claims in published maps and institutional affiliations.